Advancing glioblastoma imaging: Exploring the potential of organic fluorophore-based red emissive carbon dots

Advancing Glioblastoma Imaging: Exploring the Potential of Organic Fluorophore-based Red Emissive Carbon Dots

Justin B. Domena[a] , *Braulio C.L.B. Ferreira*[a], *Emel K. Cilingir*[a], *Yiqun Zhou*[a], *Jiuyan Chen*[a], *Qiaxian R. Johnson*[c], *Bhanu P.S. Chauhan*[c], *M. Bartoli*[d], *A. Tagliaferro*[d], *Steven Vanni*[b e f], *Regina M. Graham*[b g], *Roger M. Leblanc*[*a]

Author Address

[a] Department of Chemistry, University of Miami, Coral Gables, FL 33146, USA

[b] Department of Neurological Surgery, Miller School of Medicine, University of Miami, Miami, FL 33136, United States

[c] Department of Chemistry, William Paterson University of New Jersey, 300 Pompton Rd, Wayne, NJ 07470, USA

[d] Department of Applied Science and Technology, Politecnico di Torino, Italy

[e] HCA Florida University Hospital, 3476 S University Dr., Davie, FL, 33328

[f] Department of Medicine, Dr. Kiran C. Patel College of Allopathic Medicine, Davie, USA.

[g] Sylvester Comprehensive Cancer Center, University of Miami Miller School of Medicine, 1475 NW 12th Ave, Miami, FL, 33136, USA

* Corresponding author: rml@miami.edu

Keywords

carbon dots, red emission, cell imaging, glioblastoma, blood brain barrier

Abstract

Over time, the interest in developing stable photosensitizers (PS) which both absorb and emit light in the red region (650 and 950 nm) has gained noticeable interest. Recently, carbon dots (CDs) have become the material of focus to act as a PS due to their high extinction coefficient, low cytotoxicity, and both high photo and thermal stability. In this work, a Federal and Drug Association (FDA) approved Near Infra-Red (NIR) organic fluorophore used for photo-imaging, indocyanine green (ICG), has been explored as a precursor to develop water-soluble red emissive CDs which possess red emission at 697 nm. Furthermore, our material was found to yield favorable red-imaging capabilities of glioblastoma stem-like cells (GSCs) meanwhile boasting low toxicity. Additionally with post modifications, our CDs have been found to have selectivity towards tumors over healthy tissue as well as crossing the blood-brain barrier (BBB) in zebrafish models.

1. Introduction

The utilization of red emission in the phototherapeutic window (650-950 nm) for bio-imaging and photo-therapeutics involves the exploitation of exciting chromophores located on the PS[1]. A key feature of the far-red range of excitation stems from the fact that there is an increase of light penetration in tissues. Unfortunately, current commercial PS which use excitation wavelengths outside the phototherapeutic window have their light absorption dampened by light scattering or

reflection of light by the host's tissue[2–4]. To achieve optimal efficiency, PS used in theranostics techniques require the utilization of light within the red region to (NIR-I) window ranging between 650-950 nm, respectively[5]. A direct consequence of this requirement results in the degradation of the PS such as photobleaching or thermal degradation[6,7]. Additionally, modern PS have the disadvantage of low blood clearance from the host which limits biomedical applications[8]. Significantly, CDs have attracted increasing attention in various biomedical areas of application such as *in vitro/in vivo* imaging, biosensor, drug delivery, photodynamic therapy, and photothermal therapy[9–17]. This interest is due to their characteristic of being free of metals, having relatively low cytotoxicity in animal models, and boasting both high photo and thermal stability[18,19,28,29,20–27]. Up to date, there has been a scarcity of literature that focuses on water-soluble, red emissive carbons dots past 650 nm suitable for biological studies. Xiong and coworkers have explored the synthesis of red emissive CDs through a bottom-up approach using a hydrothermal one-pot synthesis of red emissive CDs using urea and p-phenylenediamine as precursors in 50 mL of water at 160ºC for 10 hrs[30]. The CDs, when purified via silica column chromatography resulted in products with a wide emission range from 440 to 625 nm. The rationale behind this characteristic was attributed to the increase of oxygen species on the CD's surface which effectively lowers the band gap of the CDs causing a bathochromic shift towards the lower red region at 625 nm. The data demonstrated that the surface chemistry of CDs plays a pivotal role in elucidating red emission. Further works by Zheng et al. suggest that complex surface modifications of produced CDs with cyanine-based dyes are of interest to unlock the potential route to develop red emissive CDs[31]. Although promising, the previous work mentioned fails to produce red emissive CDs which are also water-soluble. In our work, we posit a variety of synthetic pathways for the formation of CDs derived from ICG, citric acid, and

PEG which leads to an enhanced bathochromic shift to produce amphiphilic CDs with highly valuable emission in the red region. Our materials are ideal candidates for study as a NIR PS in systems both *in vivo* and *in vitro*.

Glioblastoma (GBM) is a grade IV astrocytoma and is the most common malignant brain in adults. Accounting for 1.35% of all cancer incidents, GBM is responsible for 4% of cancer related deaths yearly with a survival median of 15 months[32–34]. Therapy can fail in treating GBM due to various reasons. These include the difficulty of surgically removing the entire tumor, limitations in the effectiveness of anti-cancer drugs in reaching the brain, and the presence of treatment-resistant GSCs. This subpopulation of GBM tumor cells exhibit early tumor progression, aggressive invasion into the surrounding brain parenchyma, and chemo-resistance due in part to the overexpression of multidrug resistance pumps (P-glycoproteins), which leads to increased efflux of drugs as well as imaging agents from the tumor cells[32–40]. It has been well-documented that the extent of tumor resection directly correlates with patient outcome[41]. To optimize tumor resection and patient outcome, surgeons are exploring fluorescence guided surgery in which the tumor cells are fluorescently labeled in order for the surgeon to visualize tumor cells especially at the leading edge of the tumor. The use of 5-aminolevulinic acid (5-ALA) is increasing in the clinical area[42,43]. 5-ALA is a non-fluorescent precursor to heme and is converted to the fluorescent product protoporphyrin IX (PpIX) in tumor cells. However, PpIX has its limitations as both photobleaching and variations of the concentration levels within the tumor. The tumor core normally presents much brighter fluorescence when compared to the leading edge as well as between patients with very low fluorescence observed in lower grade astrocytomas[44]. Therefore, the development of novel photo-stable imaging agents that can target both bulk tumor cells and GSCs is necessary to achieve the most efficient success rate[45–47]. The

ideal fluorescent agent would demonstrate high selectivity toward tumor cells, high sensitivity to improve contrast between tumor and normal tissue and low toxicity.

In this work, an (FDA) approved hydrophilic cyanine-based dye, namely ICG, was explored as a model precursor to develop red emissive CDs (R-CD). ICG was selected as the precursor of choice due to the wide scope of clinically excellent properties such as low toxicity, efficient binding to blood lipo-proteins, short lifetime in blood circulation, and usability in the tissue optical window (NIR) region[48–51]. Herein, we hypothesize that it is possible to develop hydrophilic CDs from ICG. Furthermore, it is expected that the CDs will retain most of the functionality of the precursor such as favorable optical behavior in the far-red region to effectively image tumor cells. CDs have several advantages over other red-emissive organic dyes. They demonstrate high resistance to photobleaching, strong absorption in the red/NIR region and are biodegradable. In comparison, ICG, another red-emissive material, suffers from poor chemical and optical stability, as well as mediocre photothermal properties. Recent studies found that CDs derived from NIR dyes such as ICG exhibit significantly improved thermal stability and resistance to photobleaching compared to ICG[52]. Moreover, their photothermal properties were greatly enhanced. The CDs showed a wider functional pH range, a 50% improvement in photothermal conversion efficiency, and superior photothermal cyclability. These findings indicate that CDs have the potential for more effective and stable applications in various fields. In our work, R-CDs derived from ICG modulate BBB penetration and tumor homing capabilities depending on peptide-surface functionalization. To our knowledge, this work is the first account of far-red emissive CDs in purely water-based application.

2. Experimental Section

2.1 Materials

ICG (>99% purity) and polyethylene glycol 1000 (PEG1000, >99% purity) were procured from Sigma-Aldrich (St. Louis, MO). Anhydrous citric acid (BDH, 99.5% purity) was obtained from VWR (West Chester, PA). Nine residue peptide LINTT1 (AKRGARSTA) 94.5% purity was obtained from LifeTein (Somerset, NJ). Transferrin (>98% purity) from human blood plasma was obtained from Sigma-Aldrich (St. Louis, MO). Dialysis tubing with molecular weight cutoff (MWCO) of 3500 was bought from Thermo Scientific (Rockford, IL). Deionized (DI) water used was ultrapure (type I) water which was purified using a Millipore Direct-Q 3 water purification system acquired from EMD Millipore Corp. The purified water displayed a surface tension of 72.6 mN m^{-1}, a resistivity of 18.2 MΩ cm and a pH value of 7.0 ± 0.3 at 20.0 ± 0.5 °C. All the chemicals were used as received. The human pediatric glioblastoma cell line (SJ-GBM2) was obtained from Children's Oncology Group (COG, Texas Tech University, Health Science Center, TX, USA) and maintained in RPMI media supplemented with 10% Fetal bovine serum (FBS) and 1% penicillin-streptomycin (P/S). Human mesenchymal stem cells (MSCs) were maintained in MEM alpha supplemented with 20% FBS and 1% P/S. Glio3, Glio9 and Glio38 are GSCs derived from patient's resected tumors following patient consent and Institutional Review Board (IRB) approval[53–55].GSCs were maintained in neural stem-cell media consisting of DMEM/F12 3:1 supplemented with 20 ng/mL each of epidermal growth factor (EGF) and fibroblast growth factor (FGF), 2% Gem21 and 1% P/S. All cell culture reagents were obtained from ThermoFisher Scientific except for EGF, FGF and Gem21 which were obtained from Gemini Biosciences. All cell lines were routinely tested for mycoplasma using LookOut

mycoplasma PCR detection kit (Sigma Aldrich, St. Louis, MO, USA) according to the manufacturer's instructions and maintained at 37 °C in a humidified 5% CO_2 incubator.

2.2 Synthesis of R-CDs

The R-CDs were obtained by means of microwave pyrolysis of citric acid (0.200 g), ICG (0.005 g), and PEG1000 (0.050 g). To preface, the precursors were dispersed in a beaker containing 15 mL of DI water ultrapure (type I) and sonicated for 1 min to ensure a homogenous mixture which was observed to be a vivid light-green color. The solution of starting material was then placed in the microwave and set for 150 s at a power setting of 700 W. Post pyrolysis, it was observed that the solution remained with roughly 5 mL of water with a dispersion of dark green colored solubilized product. The solution was then collected and centrifuged for 30 min at 10,000 RPM for three cycles to remove large, suspended particles. The remaining supernatant was then placed within a 3500 MWCO Snakeskin dialysis for 72 hrs in deionized (DI) water ultrapure (type I), with the water changed every 12 hrs. The purified solution of R-CDs was then frozen at -40ºC for 24 hrs and sequentially set for lyophilization for 72 hrs, producing a free-flowing dark green powder. These freeze-dried R-CDs were then used for study.

2.3 R-CD-Ligand conjugations via carbodiimide (EDC/NHS) coupling

Both AKRGARSTA and transferrin (R-CD-AKRGARSTA and R-CD-Transferrin, R-CD-Tf) conjugates were synthesized by carbodiimide coupling which was feasible due to the abundance of carboxylic acids functional groups on the surface of the CD. This conjugation

involves the primary amine group of either the nine-residue sort peptide AKRGARSTA or transferrin, which can form a stable amide bond. First, 50.0 mg of R-CD was solubilized in 10 mL of Phosphate-buffered saline (PBS, pH 7.4) and allowed to stir for 30 min. To proceed with the activation of -COOH groups on the surface of R-CD, 63.9 mg of 1-ethyl-3-(3-dimethylaminopropyl) carbodiimide (EDC) was transferred into 5 mL of the same buffer within a vial and mixed to ensure a homogeneous mixture. Additionally, 193.2 mg of N-hydroxy succinimide (NHS) was also transferred into another vial containing 5 mL of the same buffer and mixed. Sequentially, both EDC and NHS were aliquoted in 1 mL increments to the solution containing the R-CDs and were allowed to stir for 30 min. To synthesize the conjugate of interest (R-CD-AKRGARSTA or R-CD-Tf), either 7.2 mg of AKRGARSTA or 20 mg of transferrin was solubilized in a separate vial containing 5 mL PBS buffer and was aliquoted in 1mL increments of the mixture of R-CD, EDC, and NHS. The resultant mixture was then allowed to stir for 48 hrs while protected from light. This process allows the conjugation from the -COOH group on the surface of the R-CD and the $-NH_2$ of the ligand of interest. The newly formed CD conjugate was then purified by dialysis against ultra pure water for 72 hrs to allow unreacted small molecules to exit from the dialysis membrane with 3500 Da MWCO. Finally, the purified R-CD-AKRGARSTA was lyophilized to yield a dark green powdered product. Successful conjugation was confirmed by circular dichroism spectroscopy (CDS), zeta potential (ZP), and mass spectrometry (MS) (**Figure S1**). Whereas the R-CD-Tf conjugate was lyophilized to yield a turquoise powdered product with its conjugation confirmed by photoluminescence (PL), transmission electron microscopy (TEM), Atomic force microscopy AFM, MS and ZP (**Figure S2-3**).

173

174 *2.4 Characterization*

175 UV-vis spectra were obtained from an Agilent Cary 100 UV-vis spectrophotometer. PL
176 characterization was performed on a Fluorolog HORIBA Jobin Yvon fluorometer with a slit
177 width of 5 nm for excitation and emission. All optical characterization spectra were obtained
178 with quartz cells possessing an optical pathlength of 1 cm. Fourier-transform infrared (FTIR)
179 spectroscopy data were obtained with a PerkinElmer FTIR (Frontier) spectrometer (Waltham,
180 MA, USA) by using the attenuated total reflection (ATR) technique with air as background.
181 AFM images of CDs were obtained with an Agilent 5420 AFM (Santa Clara, CA, USA). To
182 perform AFM measurement, a drop of diluted CDs aqueous solution was applied on a clean
183 silica mica slide and air dried, which then was transferred to do the screening using tapping
184 mode. The tips used were silicon tips (length: 225 μm; thickness: 5 μm) manufactured from
185 Nanosensors with a force constant of 15 N/m. TEM was performed by using a JEOL 1200X
186 TEM (Peabody, MA, USA). For TEM measurements, a drop of the R-CDs solution was placed
187 on a carbon coated copper grid and air dried prior to examination. The ZP was recorded on a
188 Malvern Zetasizer nano-series. The thermogravimetric analysis (TGA) and derivative
189 thermogravimetric analysis (DTG) of R-CDs and some precursors were conducted using a
190 thermo-microbalance (TG 209 F3 Tarsus, Netzsch, USA) while heating under a flow of nitrogen
191 gas from 40 to 1000 °C at a rate of 10 °C/min. Raman spectra were recorded using a Renishaw
192 Inviah Spectrometer equipped with a
193 blue (457 nm), green (514.5 nm), and red (wavelength 785 nm) laser source and a 50x objective.
194 Applied power using green laser source was in the range of 10 to 100 μW, with the red laser line
195 from 50 to 500 μW and for the blue laser line from 100 μW to 1 mW. X-ray photoelectron

196 spectroscopy (XPS) spectra were recorded by using a PHI 50 0 0 Versaprobe (Physical
197 Electronics, Chanhassen, MN, USA) scanning X-ray photo electron spectrometer
198 (monochromatic Al K-alpha X-ray source with 1486.6 eV energy, 15 kV voltage, and 1 mA
199 anode current). The circular dichroism experiment was run under room temperature on the Jasco
200 (J-810) Circular Dichroism Spectropolarimeter. To obtain a good S/N ratio during the CDS
201 analyses, 100 µg/mL was used as the concentration of all samples (R-CD, RCD-AKRGARSTA,
202 and R-CD-Tf) in water as solvent; standard sensitivity; 100 nm/min scan speed; 1 nm band
203 width; 1 s response time; 0.5 nm data pinch and 5 accumulation scans.

204 *2.5 Cell Viability*

205 Cell viability was determined using the CellTiter 96® Aqueous One Solution Cell
206 Proliferation Assay (MTS) (Promega Madison, WI, USA). R-CDs were dispersed in phenol red-
207 free DMEM cell culture media at a concentration of 10 mg/ml. SJ-GBM2 cells and MSCs were
208 plated at a density of 1 x 10^5 and 0.5 x 10^5 cells/ml, respectively. GSC cell lines were plated in
209 neural stem cell proliferation media supplemented with 5% FBS at a density of 1.5 x 10^5
210 cells/ml. The following day cells were treated with 1-500 ug/ml and viability determined 72 hrs
211 later. Data is presented as percent viability compared to non-treated controls.

212 *2.6 Cell Imaging*

213 To facilitate cell adhesion, Glio3, Glio9 and Glio38 cells were plated in a media
214 supplemented with 5% FBS at a concentration of 1 x 10^6 cells/ml. At 24 hrs later, cells were
215 exposed to increasing concentrations of R-CDs (50-1000 ug/ml) for 6 hrs. To determine the
216 cellular location of R-CDs, Glio3 and Glio38 cells were treated with 500 ug/ml for 1 hour. Cells
217 were washed with PBS and treated with 4% paraformaldehyde for 30 min, washed again in PBS

and cover slips mounted using Prolong Gold Antifade reagent with and without 4′,6-diamidino-2-phenylindole (DAPI). Images were obtained using a Floid Cell Fluorescent Microscope (Thermo Fisher Scientific, Waltham, MA). For R-CD washout experiment, Glio 3 and Glio 38 neurospheres were treated with 100 ug/ml R-CDs for 4 hrs. For R-CD washout, cell culture media was removed and neurospheres washed with PBS to remove any remaining R-CDs and incubated for an additional 48 hrs in fresh media. Alternatively, the neurospheres were washed and fixed immediately following treatment (0 hrs). For R-CD peptide experiments, GSCs and MSCs were treated with equimolar concentrations of R-CDs or R-CD- AKRGARSTA for 1 hour and imaged following PBS washes and fixation as described above.

2.7 Image analysis

ImageJ was used to quantify the fluorescence intensities of to evaluate CD uptake according to literature[56]. First, images of GSC and MSCs incubated with the respective CD were median filtered to calculate an overall background value of each image, respectively. The region of interests (ROIs) for each image was detected by binarizing the images using an adaptive threshold value determined by a fixed percentile value of fluorescence intensities. Then, a weighted-fluorescence intensity was calculated for each image as follows in **Eq.1.**

$$\text{Mean fluorescence} = \frac{\sum_{1}^{N}[(\text{FI}_{\text{ROI},i} - \text{Bg})A_{\text{ROI},i}]}{\sum_{1}^{N} A_{\text{ROI},i}} \qquad \textbf{(Eq.1)}$$

FI_{ROI} is the average fluorescence intensity from a given ROI, Bg is the background fluorescence intensity, A_{ROI} is the area of a given ROI. Mean fluorescence intensity was calculated for all control and treatment groups.

To further quantify the fluorescence to as an increase in fold, the corrected total cell fluorescence (CTCF) was calculated. The CTCF was obtained by first outlining the cell of interest and their respective background. These acquired measurements enable the generation of values for both the selected area and integrated density for the cell as well as the mean intensity for the background. To measure the amount of CD fluorescence within cells, the calculation of the CTCF was performed by subtracting the product of the average fluorescence in the background and the area outside the cell from the total amount of fluorescence inside the cell. This method has been described in previous literature[57–59].

2.8 Statistical Analysis

Significance was determined using Student's t-tests for all pairwise comparisons of the different treatments that were tested. All the results are presented as the mean±standard error of the mean (SEM). Significance was set at $p \leq 0.05$.

2.9 Zebrafish injection and bioimaging

Wild-type zebrafish at 5 days post fertilization were obtained from the Zebrafish Core Facility at University of Miami and anesthetized by 0.02% tricaine. Then, 20 mg/mL of CDs aqueous solution were intravascularly injected into the heart of zebrafish. After 10 min, the zebrafish were mounted with low-melting agar and observed under the Leica SP5 confocal microscope under bright field and fluorescence at excitation of 405 nm. The animal care protocol for all procedures used in this study was approved by the University of Miami Animal Care and Use Committee and complies with the guidelines of the National Science Foundation. Zebrafish studies were conducted under the procedures related to the IACUC 21-182 for the use of

zebrafish and meets the criteria for review under Section IIIF in accordance with the *NIH Guidelines*

3. Results and Discussion

3.1 Characterizations of R-CDs

The analysis of the UV-vis spectrum of R-CDs reveals typical absorption bands attributed to the π–π* transitions of the C=C bond and the n–π* transition of the C=O bond at 210 and 397 nm, respectively (**Figure 1**)[60]. Further bands found at 770 and 890 nm are reminiscent of the bands usually observed from ICG at 710 and 790 nm, respectively. These bands are normally related to nitrogen-containing heterocyclic structures which the dye is composed of. The

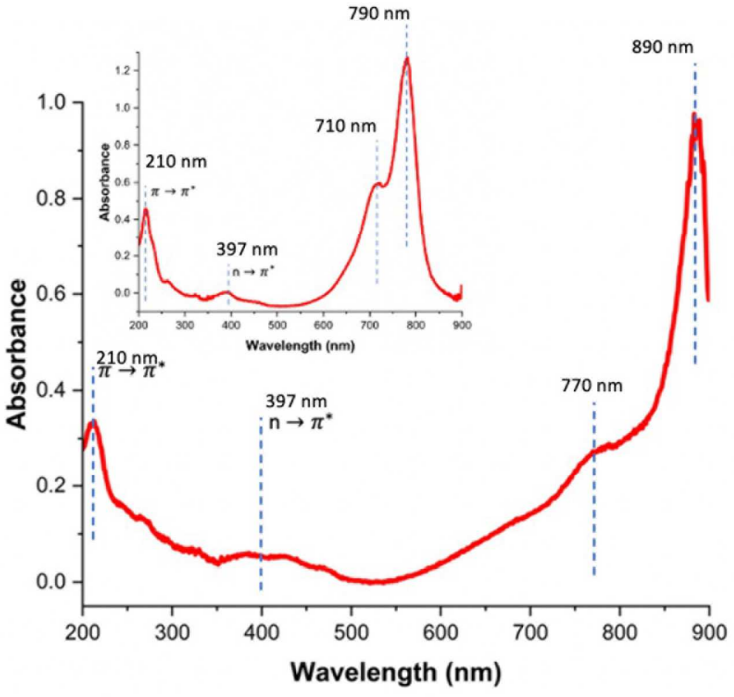

Figure 1. UV-vis analysis R-CDs, (inset) UV-vis spectrum of ICG.

bathochromic shift of the absorbance of R-CDs is hypothesized to be attributed to the increase of oxygenated groups as confirmed by FTIR due to the implementation of citric acid and PEG1000 during the synthetic process.

The PL of R-CDs was studied to assess the viability of the material in fluorescent imaging techniques across a wide range of excitations. The expected result was to produce CDs that retained optical properties similar to ICG which has notable emission peaks at 599 and 815 nm, respectively. It was hypothesized that there may be degradation of the dye during the synthetic process resulting in slight loss of conjugation, leading to an increase of the energy band gap producing a slight hypsochromic shift[61]. It is noteworthy that this behavior was observed in the PL of the R-CDs when they were stimulated with light between 360 to 700 nm, at 20 nm intervals (**Figure 2A**). R-CDs were found to possess red emission at 697 nm as well as a 599 nm emissive peak similar to the ICG dye (**Figure 2B**). Interestingly, R-CDs were found to have a clear isosbestic point at both 575 and 665 nm. These findings support a uniformity on the PL profile across a long range of the visible spectrum. This discovery holds significant implications as it suggests that the optical characteristics of the R-CDs will remain consistent across a specific range of wavelengths owing to their uniformity. We hypothesize, during the synthesis of R-CD, the electronic structure of the ICG molecule is partially preserved and is interconnected via PEG chains. This results in the production of CDs that have similar excitation and emission properties as the dye precursors.

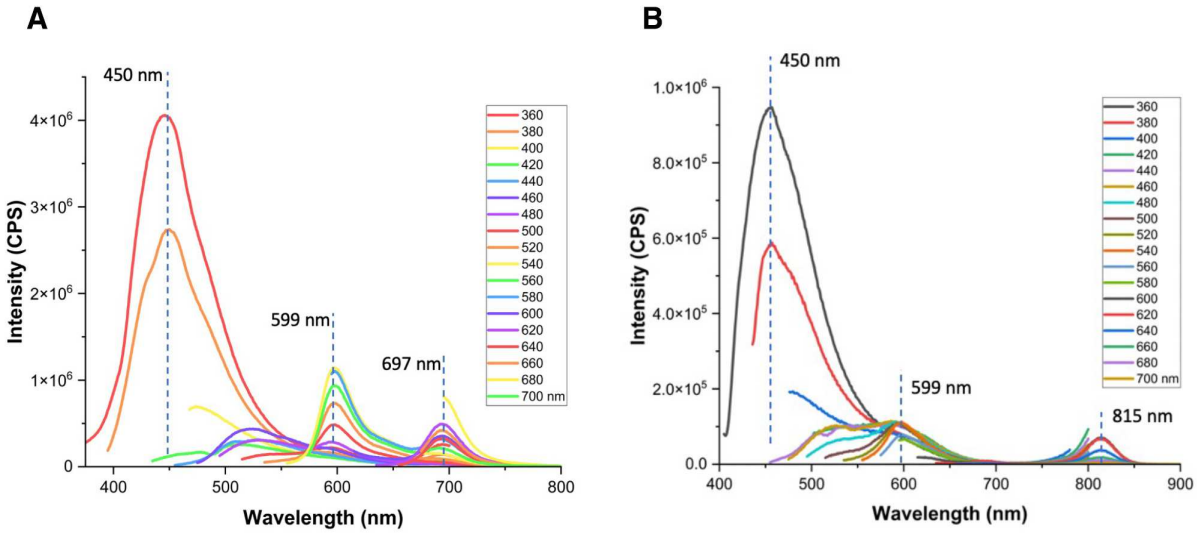

289 **Figure 2.** Optical analysis of R-CDs. (A) R-CD PL spectrum, (B) ICG PL spectrum.

290 FTIR is a suitable technique for revealing the surface functionality of CDs, which typically
291 consists of functional groups containing oxygen and nitrogen. Moreover, FTIR has the unique
292 ability to penetrate to a depth of 2 µm, making it a powerful tool for qualitative analysis of both
293 the surface and core of CDs. A comparative analysis of R-CDs and the starting material was
294 performed to reveal a glimpse into the surface of the CD (**Figure 3**). Stretching vibrations are
295 1700 cm^{-1} are due to presence of C=O bonds on the surface of the CD. Upon deeper analysis of
296 R-CD, the intense peaks at 1335 and 1277 cm^{-1} are due to the asymmetric S=O and C-N
297 stretching vibrations, respectively. This characteristic supports the presence of moieties from the
298 ICG dye, which have the same respective peaks. Between 3000 and 3100 cm^{-1} one would expect
299 to observe the C-H stretching of the alkenes which make up the carbonized network of R-CDs,
300 though increased spectral broadening from the carbonized network diminishes an observable
301 peak. Additionally, the broad peak in between 3300 and 3580 cm^{-1} are attributed to stretching
302 vibrations of O–H groups present as well as the medium peak at 2850 cm^{-1} indicative of C–H
303 stretching vibrations of alkane groups due to the PEG1000 present during the synthetic process,

confirming the availability of these groups on the surface of the R-CDs, respectively. The peaks at 1085 and 1205 cm^{-1} can be ascribed to –C–O– and C–OH groups on the surface of the R-CDs, respectively. These results suggest that R-CD retains most functionality from ICG which passivates the surface[62]. Additionally, through the implementation of PEG1000 during the synthetic procedure, increased -OH functional groups are to be found on the surface of the CD. It is hypothesized the abundance of these groups is responsible for the high solubility of R-CDs in water[63].

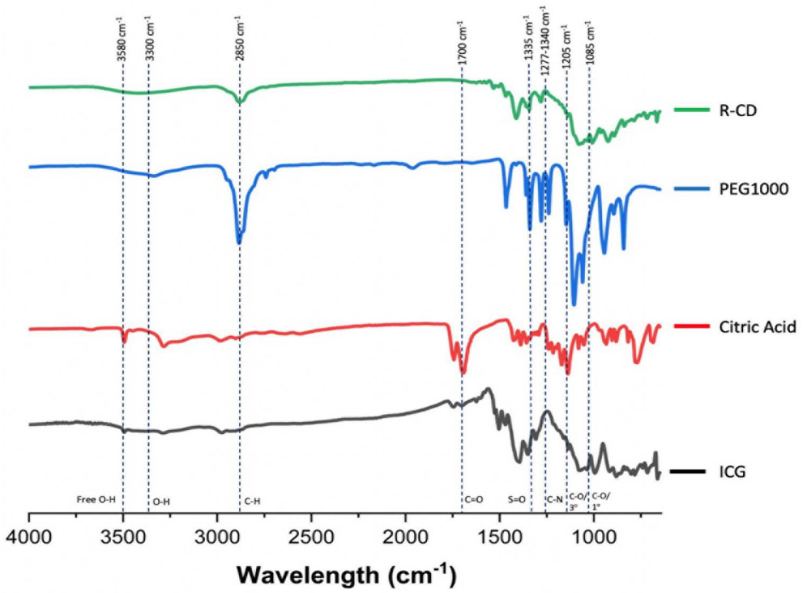

Figure 3. FTIR spectral analysis of R-CD, PEG1000, Citric Acid, and ICG.

Functional moieties can be identified and quantified by TGA and DTG measurements by their different and discernible decomposition temperatures. TGA and DTG of citric acid were previously provided, so they are not shown in **Figure 4**[64]. In general, the TGA of R-CDs and PEG (**Figure 4A**) show a similar thermal decomposition trend across different temperatures, which demonstrates a structural similarity between R-CDs and PEG, as a result of the use of PEG during the synthesis of R-CDs. Also, it is worth noting that an estimated 10% residue

remained after the decomposition of ICG. Considering the structure of ICG containing Na^+ and -SO_3^-, the remnant is likely to be Na_2SO_3 (8%) or Na_2SO_4 (9%), which basically matches the 10% residue mass percentage. Upon dialysis, the R-CDs no longer retained Na+ ions, resulting in the absence of any residual signal in the TGA analysis of the R-CDs. In addition, the DTG results display noticeable differences and similarities between R-CDs and their precursors (**Figure 4B**): (1) ICG has five decomposition stages: 40-177, 177-268, 268-368, 368-544 and 544-828 °C; (2) PEG has three decomposition steps: 40-138, 138-419, and 419-514 °C; (3) the R-CDs possess five decomposition periods: 40-172, 172-248, 248-403, 403-523 and 523-1000 °C; (4) the DTG of PEG and R-CDs are somewhat similar; (5) the thermal stability of R-CDs is higher than ICG, PEG and citric acid considering an enhanced highest decomposition temperature, which might benefit from a higher carbonization degree that resulted from the hydrothermal treatment during the CD synthesis; (6) with the DTG of a well-established CD species as a reference,[65] any peaks between 40-122 °C indicate the loss of water molecules (moisture). The mass loss at 122-168 °C suggests the loss of water molecules formed through intramolecular dehydration condensation reactions[66]. The stage between 168-250 °C is ascribed by the decomposition of edge-plane oxygen-containing functional groups such as epoxy, carboxyl and carbonyl groups[67]. The stage at 250-338 °C is due to the decomposition of some relatively stable oxygen-containing functional groups and sublimation of small carbon frameworks. The stage at 338-448 °C indicates the decomposition of amines[68,69]. Eventually, the stage at 448-1000 °C indicates the decomposition of graphene-like structures[70–72]; (7) thus, in the first stage, PEG (40-138 °C) showed a desorption of moisture while ICG (40-177 °C) and R-CDs (40-172 °C) exhibited the loss of water molecules from moisture and formed through intramolecular dehydration condensation reactions. However, ICG doesn't contain hydroxyl groups so the mass loss for ICG is hypothesized to be primarily

moisture desorption; (8) the second decomposition stages of ICG (177-268 °C) and R-CDs (172-248 °C) are similar with a mass loss of 9 and 10%, respectively, due to the decomposition of edge-plane oxygen-containing functional groups such as epoxy, carboxyl, and carbonyl groups. Nevertheless, the only edge-plane oxygen-containing functional group in ICG is $-SO_3$, so this DTG peak is likely to indicate the loss of $-SO_3$, which can be confirmed by the mass percentage (10%) of $-SO_3$ in ICG (***Note:*** one $-SO_3$ will be left to form Na_2SO_3 or Na_2SO_4). Additionally, in this temperature range, citric acid is transformed into aconitic acid, itaconic acid and anhydrous itaconic acid while releasing CO_2 and water molecules, so it is hard to identify that the mass loss of R-CDs is due to the release of CO_2 or SO_2 solely based on the DTG measurement. In comparison, the second decomposition stage of PEG was extended to 419 °C. Given the simple unit-repeated structure of PEG, the dramatic mass loss (97%) during the second stage of 138-419 °C shows the breakdown of the unit-repeated oxygen-containing backbone; (9) the decompositions of relatively stable oxygen-containing functional groups and carbon frameworks were observed in the third decomposition stage (248-403 °C) of R-CDs and the corresponding mass percentage in R-CDs is 82%. On the contrary, due to the lack of oxygen-containing functional groups in ICG, the mass loss (13%) at 268-368 °C was hypothesized to occur due to the decompositions of short alkane and alkene chains. A similar mass loss at this stage between R-CDs and PEG also suggests a similarity in the structure; (10) due to the presence of amines, ICG (368-544 °C) and R-CDs (403-523 °C) possess a fourth decomposition stage with a mass loss of 21 and 9%, respectively. However, since amines are incorporated in aromatic structures, the highest decomposition temperatures of at least ICG were raised together with the mass loss compared to the theoretical amine contents; (11) compared to PEG and citric acid, given the aromatic rings in the structure of ICG, the dramatic decomposition of ICG occurred at the last

stage of 544-828 °C with a mass loss of 39%. Meanwhile, R-CDs also showed a mass loss of 5% corresponding to the decomposition of graphene-like structures in the core; (12) according to the contents of oxygen-containing carbon frameworks (82%) and aromatic rings (5%) inherited from PEG (MW: 1000 Da) and ICG (MW: 775 Da), respectively, the structure of 1 mole R-CDs (MW: 966 Da) is hypothesized to be composed of 1 mole PEG (incomplete), 1 mole ICG (incomplete) and an unknown amount of citric acid (incomplete).

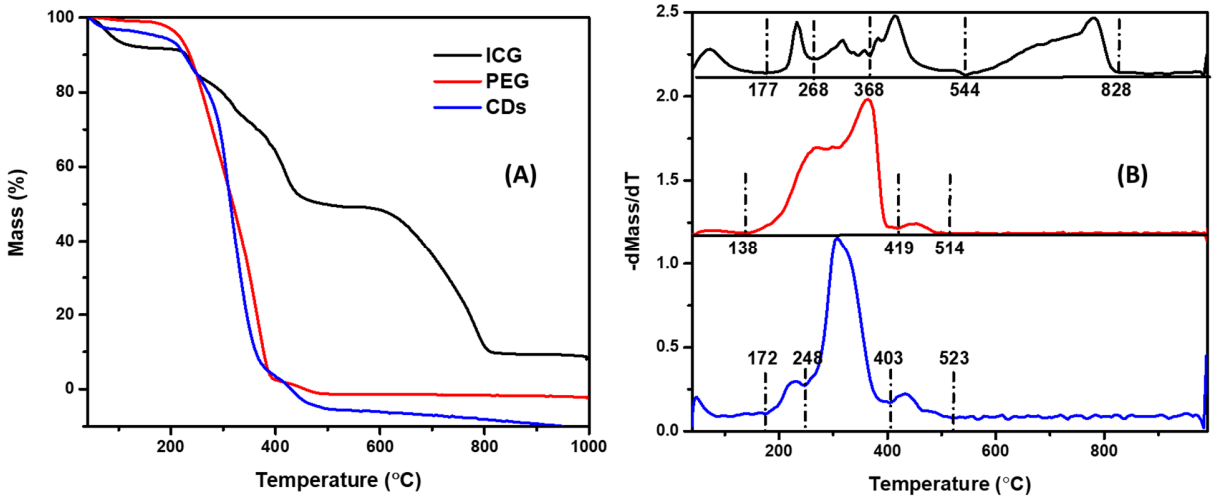

Figure 4. TGA (A) and DTG (B) of R-CDs and some precursors including ICG and PEG.

Raman spectroscopy is a facile and non-destructive technique that can be used to characterize the crystallinity and chemical functionality of graphitic materials, as well as to elucidate defects. As a powerful tool for investigating the disorder and crystallinity of CDs, Raman spectroscopy can help to determine the level of disorder present in CDs, which plays a crucial role in their electronic and optical properties. By using Raman spectroscopy to understand the degree of disorder and crystallinity of CDs, researchers can optimize their performance for various applications such as bioimaging. For our system, we are interested in both the position and intensity of two prevalent spectral bands (D band and the G band). The G-band denotes the

amount of graphitization (sp^2 hybridization) R-CDs has and the D-band represents the degree of defects and functionalization of R-CDs such as sp^3 hybridization[73,74]. The Raman spectrum was reported in the range from 600 to 2200 cm^{-1} and fitted according to Tagliaferro et al.[75] as shown in **Figure 5**. The spectrum of R-CDs reveals two distinct peaks at 1375 (D-band) and 1585 cm^{-1} (G-band), respectively[76–78]. Additionally, the baselined fitted Raman spectrum of R-CDs shows the presence of highly disordered systems with a large D peak and broad 2D region. The intensity ratio of the peak of the G band to the D band (I_D/I_G) was up to 2.9. In graphitic material, a higher in I_D/I_G ratio indicates that the synthesized R-CDs have an increased amount sp^2 clusters in its structure[79–81].

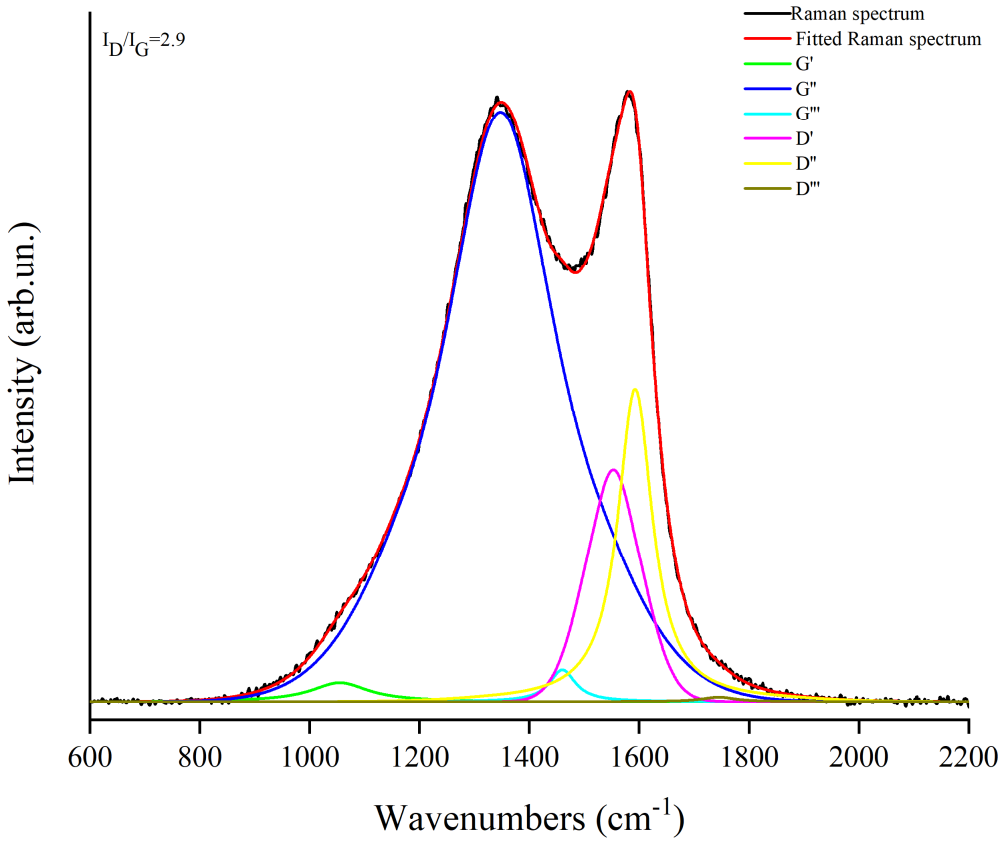

Figure 5*: Raman spectra R-CDs*

The ZP of the R-CDs was obtained to further understand the surface and the surface charge. In brief, ZP is an essential technique for characterizing the surface properties of CDs such as surface charge, stability, and functionalization. By measuring the ZP, researchers can gain valuable insights into the electrostatic interactions between the CDs and their surrounding environment. This information is crucial for understanding the behavior of CDs in various applications such as drug delivery, imaging, and sensing. Furthermore for our system, this technique is important to understand the colloidal stability of CDs in solution. Hence, a large absolute value above 20 mV has been observed to result in CDs that participate in interparticle repulsion leading to a well-dispersed colloidal solution[82,83]. The R-CDs were found to have a negative potential of -29.2 mV suggesting the presence of surface functional groups such as carboxylic and amides possibly attributed to the functionality left by ICG (**Figure S3**). Furthermore, the ZP data supports CDs high dispersibility/solubility when in solution since TEM and AFM measurements confirmed a lower percentage of agglomerations. The ZP of R-CD-AKRGARSTA was found to be -18.5 mV. This discovery is a good indication for aiding in the confirmation of the conjugation taking place as we hypothesize that the peptide shields the highly negative moieties on the surface of the R-CDs causing there to be a slightly less negative charged CD. Additionally, the ZP of R-CD-Tf reinforces the same rationale as the ZP was observed to be -18.2 mV.

TEM images were studied regarding R-CDs, R-CD-AKRGARSTA, and R-CD-Tf to understand the X−Y plane size distribution. The sample was sonicated for 15 min prior to measurements to breakdown any aggregate formation. R-CDs showed a narrow Poisson size distribution of 1.0-6.0 nm with a mean size of 2 nm (**Figure 6A**). The TEM of R-CD-AKRGARSTA had a Poisson size distribution of 1.0-6.0 nm with a slightly bigger mean size of

2.5 nm which is attributed to the peptide bound on the surface (**Figure 6B**). In following, the TEM of R-CD-Tf was found to have had a Poisson size distribution of 1.0-7.5 nm with the largest mean size of 3.0 nm (**Figure 6C**). We hypothesize this change is due to the bulky transferrin which is bound to the surface of R-CD. Each histogram for all three types of CDs comprises of a particle count of over 300 particles with a high degree of uniformity. AFM was also performed on the R-CDs to understand the height profile of the CDs in the z-axis. The AFM images display R-CD particles height within 2.0−2.8 nm, which is consistent with the

previous TEM diameter distribution confirming the quasi-spherical structure of the R-CDs. The AFM of R-CD-AKRGARSTA was found to have a particle height of 2.5-3.5 nm in agreement with the TEM. Likewise, the AFM of R-CD-Tf revealed a particle height of 2.5-4.0 nm which conforms with its TEM.

To further understand the surface chemistry, R-CDs were analyzed by using XPS (**Figure S4**) and high-resolution spectra for each relevant element (**Figure 7**) are reported together with table on the elemental composition (**Table 1**) and functionalities distribution (**Table S1**). As shown in

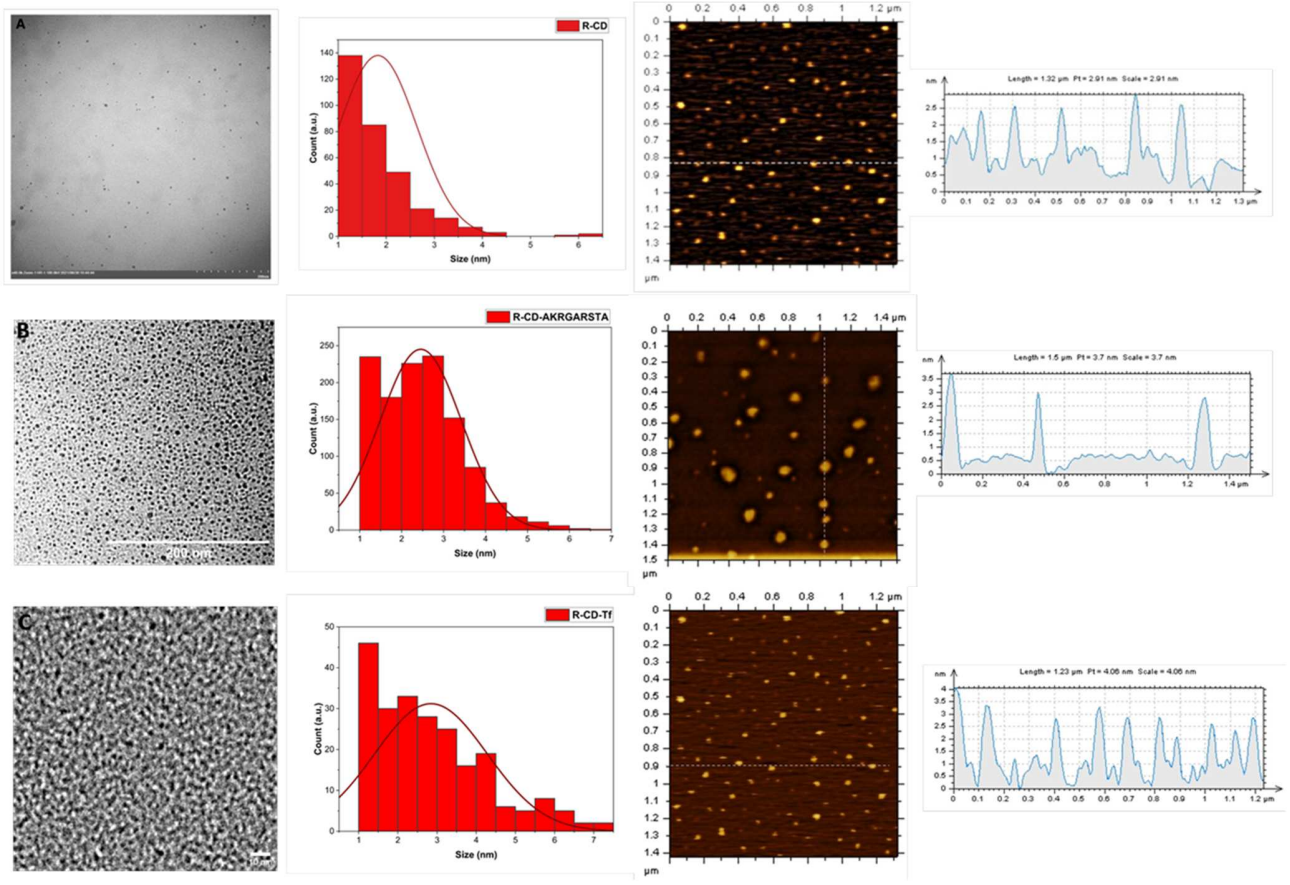

Figure 6. Morphology of R-CDs and R-CD conjugations. (A) R-CD TEM image with a scale bar of 200 nm, particle size histogram, AFM image and scale.; (B) R-CD-AKRGARSTA TEM image with a scale bar of 200 nm, particle size histogram, AFM image and scale.; (C) R-CD-Tf TEM image with a scale bar of 10 nm, particle size histogram, AFM image and scale.

Sample	Element (atom %)			
	C	*O*	*N*	*S*
R-CDs	69.5	28.9	1.1	0.5

table 1, the preliminary results of elemental composition of R-CDs show a high amount of oxygen up to 28.9 % a low content of both nitrogen (1.1 %) and sulfur (0.5 %). This was reasonably due to the massive presence of PEG chain fragments. In **Figure 7A**, R-CDs C1s spectrum showed the presence of relevant components due to sp^3 hybridized carbon (283.5 eV) and to sp^2 hybridized carbon (peaked at 284.7 eV) with an intensity of 30.1 and 52.0 %, respectively. Furthermore, C-X (X = N, O, S; 285.8 eV) is present with an intensity of up to 12.7 % while **C**OOH (289.1 eV) reaches up to 5.1 %. O1s spectrum is significantly simple with a major component due to C-O (531.3 eV) up to 90.2 % while sulphonate (532.2 eV) and COOH (533.3 eV) represent only the 6.0 and the 3.5 % respectively (**Figure 7B**). This is in good agreement with the model based on ICG fragments connected through PEG chains and residual fragments of citric acid. N1's spectrum is considerably simple (**Figure 7C**), and it is composed by one signal due to N5 (399.9 eV) as the sp^2 one that is composed by only one component due to sulphonates (166.6 eV, **Figure7D**).

Table 1: : Elemental composition of R-CDs as calculated from XPS survey spectra (average uncertainty of up $\pm$1%).

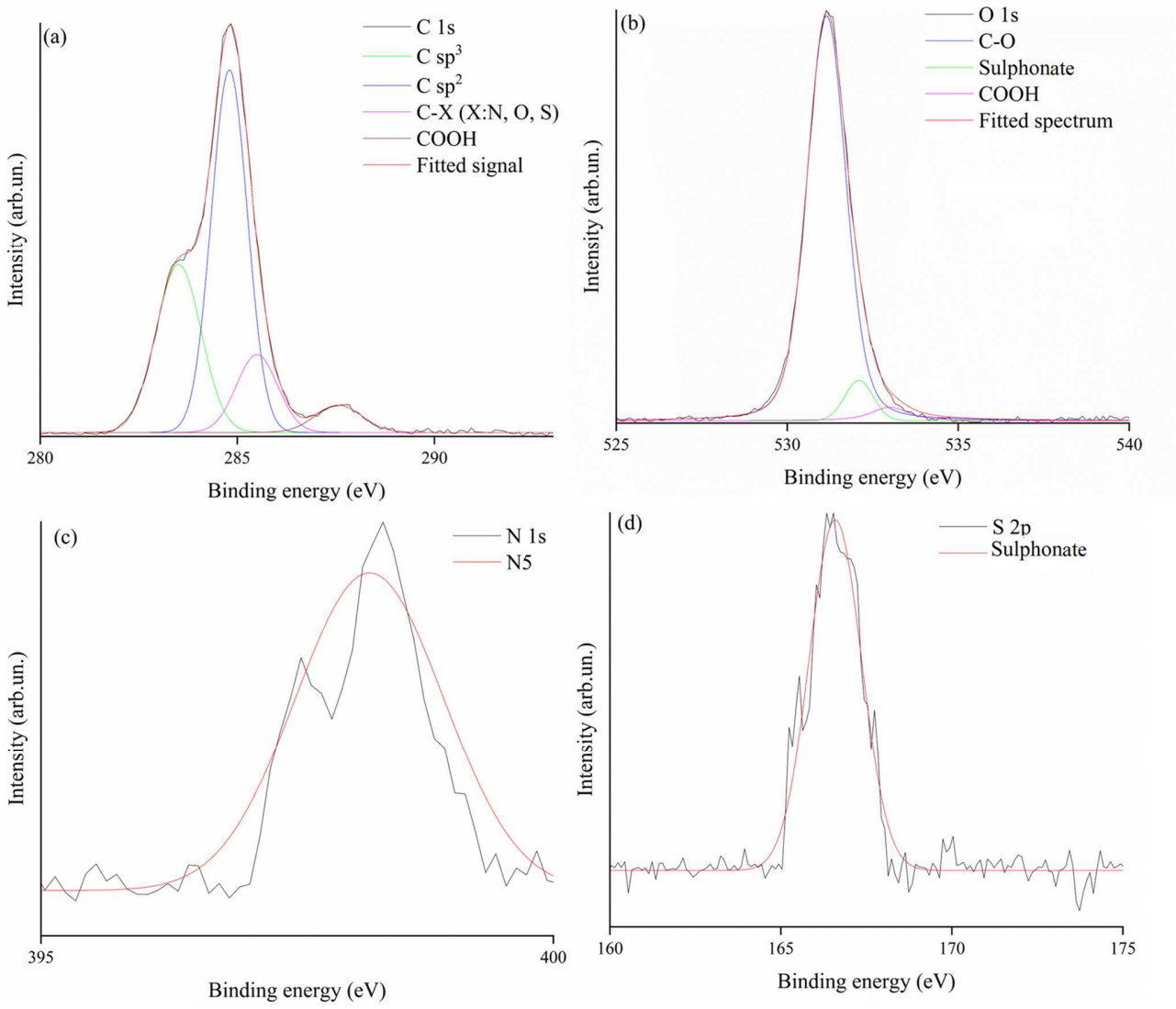

Figure 7: XPS spectra of relevant element for R-CDs.

3.2 Formation Mechanism of R-CDs

Preliminary consideration of the structure should be based on both TGA and FTIR data. As shown by TGA data, the graphitic domains are limited to only 5 wt.% of the total amount of R-CDs and there is unneglectable similarity with neat PEG suggesting the persistence of polyether chains into the final structure of R-CDs. Similarly, the FTIR spectrum of R-CDs suggests the

presence of alkyl chains together with the persistence of sulphonyl residues and the presence of small amounts of aromatic and nitrogen containing aromatic systems. Additionally, Inductively Coupled Plasma (ICP) analysis excludes the presence of sodium and Raman spectrum clearly supports the presence of highly disorganized aromatic domains. Considering the characterization data and the chemical formula of each reactant, we propose a mechanism for the formation of R-CDs that is composed by several pathways as shown in **Figure 8**.

Firstly, we can considered the hemolytic cleavage of **1** in the polyenes chain (C=C energy bond up to 255 kcal/mol[84]) producing unsaturated species **2-4**. These species could undergo through a Diels-Alder cycloaddition condensation forming chemical families like compound **5**. Another modification of **1** is the isomerization of polyunsaturated chain that connects its two 1H-benzo[g]indole units forming **6**. This species represents an interesting platform diene able to self-condense forming species such **10** that could further condense producing small condensed aromatic systems. Alternatively, **6** could undergo inter-molecular condensation with several species such as **2-4** or unsaturated citric acid derivatives (**7-8**) formed under microwave irradiation. Interestingly, cyclic anhydrides such as **13** could evolve into 4H-pyran derivatives such as **14** and **15** accounted for the aromatic oxygen moieties detected by TGA analysis. Similarly by TGA, the evolution of **8** could produce species with a naphtalenic (**21**) or biphenyl (**23**) cores. The condensed ICG derivatives formed under microwave irradiation are highly functionalized and hardly evolved to proper layered supramolecular structure as proved by the residual functionalities detected by analytical by FTIR and MS. Additionally, **24** can degrade under microwave irradiation forming low molecular weight species hydroxyl (**25**) or/and vinyl (**26**) terminated species. Hydroxyl ended chains could easily react with acidic functions, both

carboxylic and sulphonyl, forming **27** while **26** could react with both dienes forming species such as **28** and with acidic moieties forming **29**.

The PEG linked condensed ICG fragments could be schematized with a structure such the one reported in **Figure 9**. The scattering and small size of aromatic domains is in good agreement with both Raman and TGA analysis suggesting a hybrid structured in between a polymeric and layered CDs. Accordingly, aromatic clusters are surrounded by a polyether environment bonded through ester and saturated carbon-carbon bond. This could boost their local interaction through $\pi - \pi$ stacking and could be accounted for the fluorescence emission at 697 as reported for similar systems by Wang et al[85].

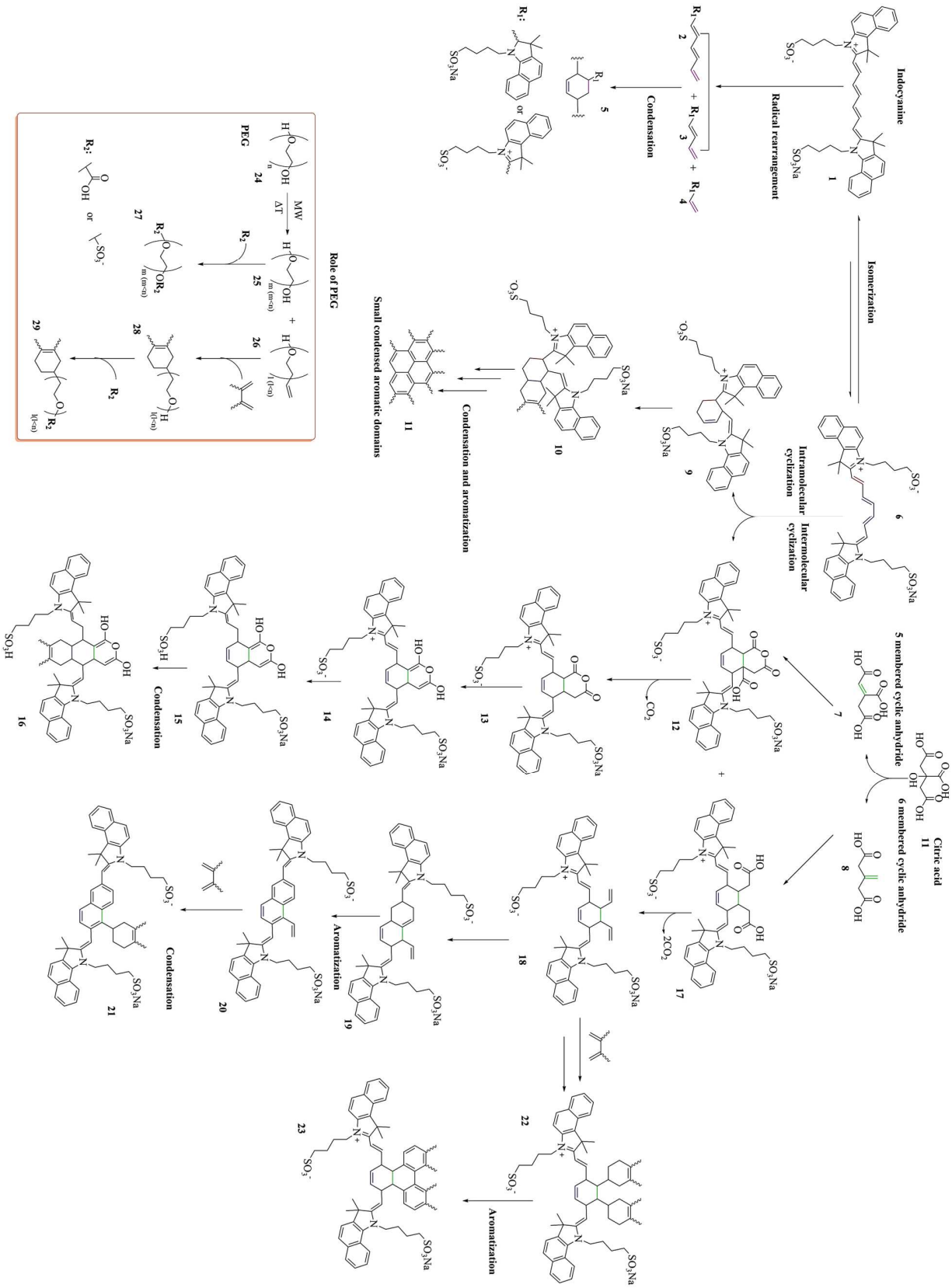

478 **Figure 8**: R-CDs formation mechanism.

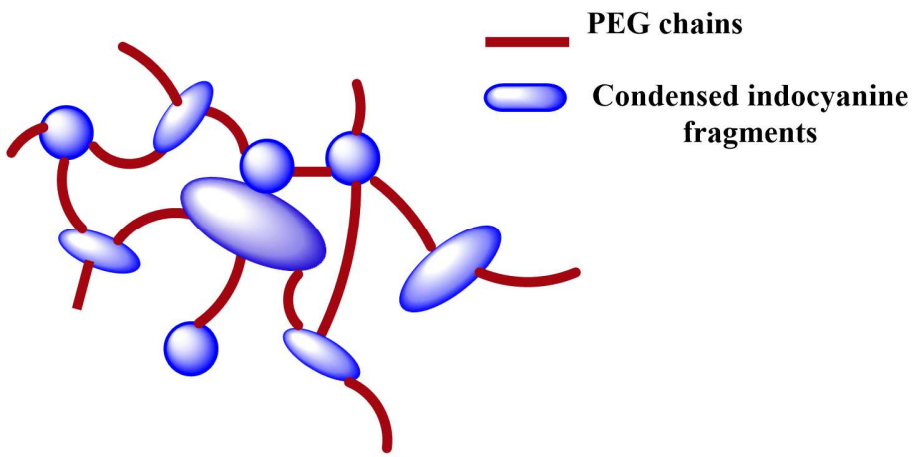

Figure 9: R-CDs structural model.

3.3 Cell Viability of R-CDs

GSCs have been shown to be resistant to current treatment modalities and are responsible for tumor regrowth following surgery. Hence, it is important to develop an imaging material that can readily undergo cellular uptake. Additionally, it is necessary that the material is non-toxic towards cells before using it for imaging applications. We anticipate that our R-CDs will have high cell viability due to the abundance of PEG on the surface, which has been proven to have excellent biocompatibility with cells[86–89]. To determine the potential biocompatibility of R-CDs, the cell viability was determined using non-tumor, and tumor cell lines: normal MSCs, SJ-GBM2 and GSCs Glio3, Glio9, and Glio38, respectively. Cells were treated with increasing concentrations (1-500 µg/mL) and cell viability was determined following 72 hrs of exposure. The R-CDs were relatively non-toxic to all cell lines especially at concentrations of 100 µg/mL or below. At drastically high concentrations of 500 µg/mL, the cell viability of MSC and SJ-GBM2 were 65 and 83% ($p > 0.05$), respectively (**Figure 10A**). This finding is important as the upper limits of concentrations for cell viability are usually presented as 100 µM[90–92]. Suggesting that within normal standards, R-CDs are highly non-toxic which is a feature of PEGylated

nanoparticles[93]. At the upper limit concentration, the cell viability for Glio3, Glio9 and Glio38 were 100, 85 and 108% ($p > 0.05$), respectively (**Figure 10B**). As expected, the R-CDs were highly bio-compatible which further reinforced the need to apply these CDs for bioimaging.

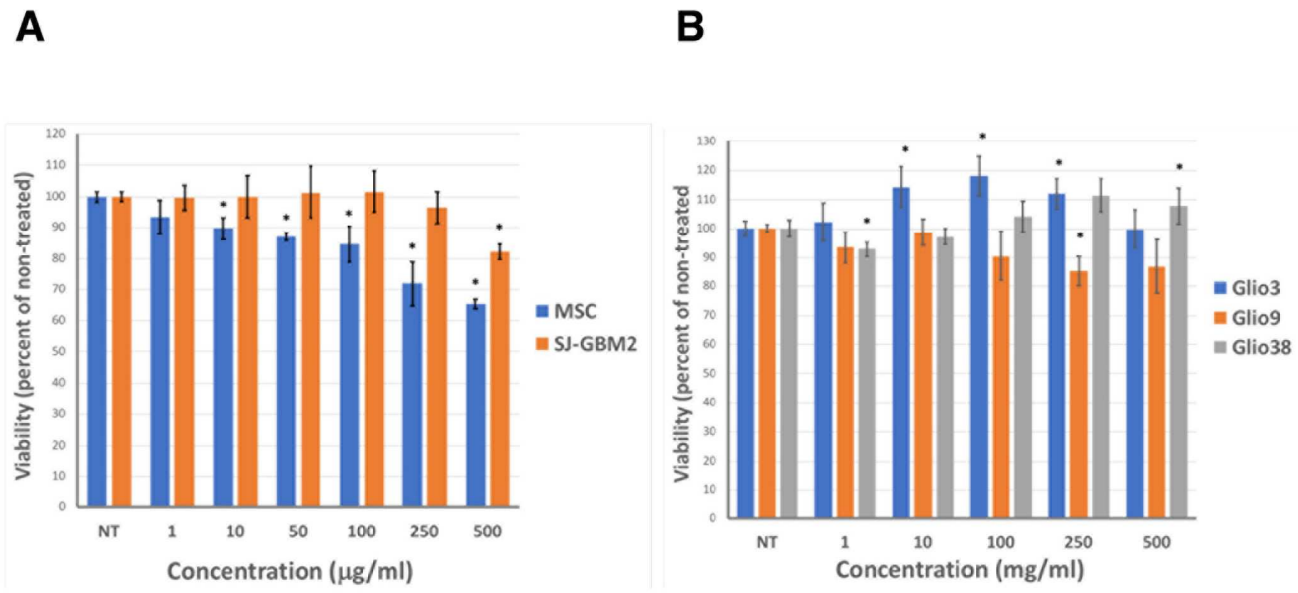

Figure 10. SJ-GBM2 and MSCs (A) and GSC lines, Glio3, Glio9 and Glio38 (B) were exposed to R-CDs at concentrations shown and viability determined by MTS assay 72 hrs later. *$p<0.05$ compared to non-treated controls.

3.4 Red Fluorescent Imaging Capabilities of R-CDs

Given the relatively low cytotoxicity observed, especially in the GBM cells, the fluorescent imaging capabilities of R-CDs were assessed. For these studies we chose to use GSCs. Cancer stem cells (CSCs) including GSCs express high levels of ATP-binding cassette (ABC) transporters which not only pump anti-cancer drugs out of the cell but many fluorescent dyes as well. In fact, CSCs are also referred to as the side population and can be isolated from tumors or

505 cancer cell lines by their ability to rapidly efflux fluorescent dyes such as Hoechst 33342. The
506 ability to fluorescently label the CSCs as well as the bulk tumor cells is necessary for maximal
507 tumor removal by fluorescence-guided tumor resection techniques. Therefore, we sought to
508 determine the potential of R-CDs to effectively label our GSC lines. Glio3, Glio9, and Glio38
509 were treated with increasing concentrations (50-1000 μg/mL) of R-CDs for 6 hrs and visualized
510 by fluorescent microscopy. Upon observation it is evident that the fluorescent intensity increases
511 in a concentration dependent manner. **Figure 11A** displays the comparison between the
512 fluorescence microscope bright field (Bf) and the red channel for non-fluorescent and fluorescent
513 cellular visualization. While no fluorescence was observed in the non-treated controls,
514 fluorescence was observed in all 3 cell lines at 100 μg/mL. As the concentration is increased to
515 an upwards of 1000 μg/mL, the fluorescence is notably stronger. Furthermore, while R-CDs
516 dispersed throughout the cell, they appeared to be localizing mainly in the cytoplasm (**Figure**
517 **11B**) since DAPI staining normally targets and highlights only the cell nucleus. Based on these
518 results, R-CDs may be well-suited for cell/tumor imaging in the red region. Additionally, the
519 favorable cell viability and imaging serves as motivation to address the challenge presented by
520 GBM, which is increased drug efflux of theranostic materials.

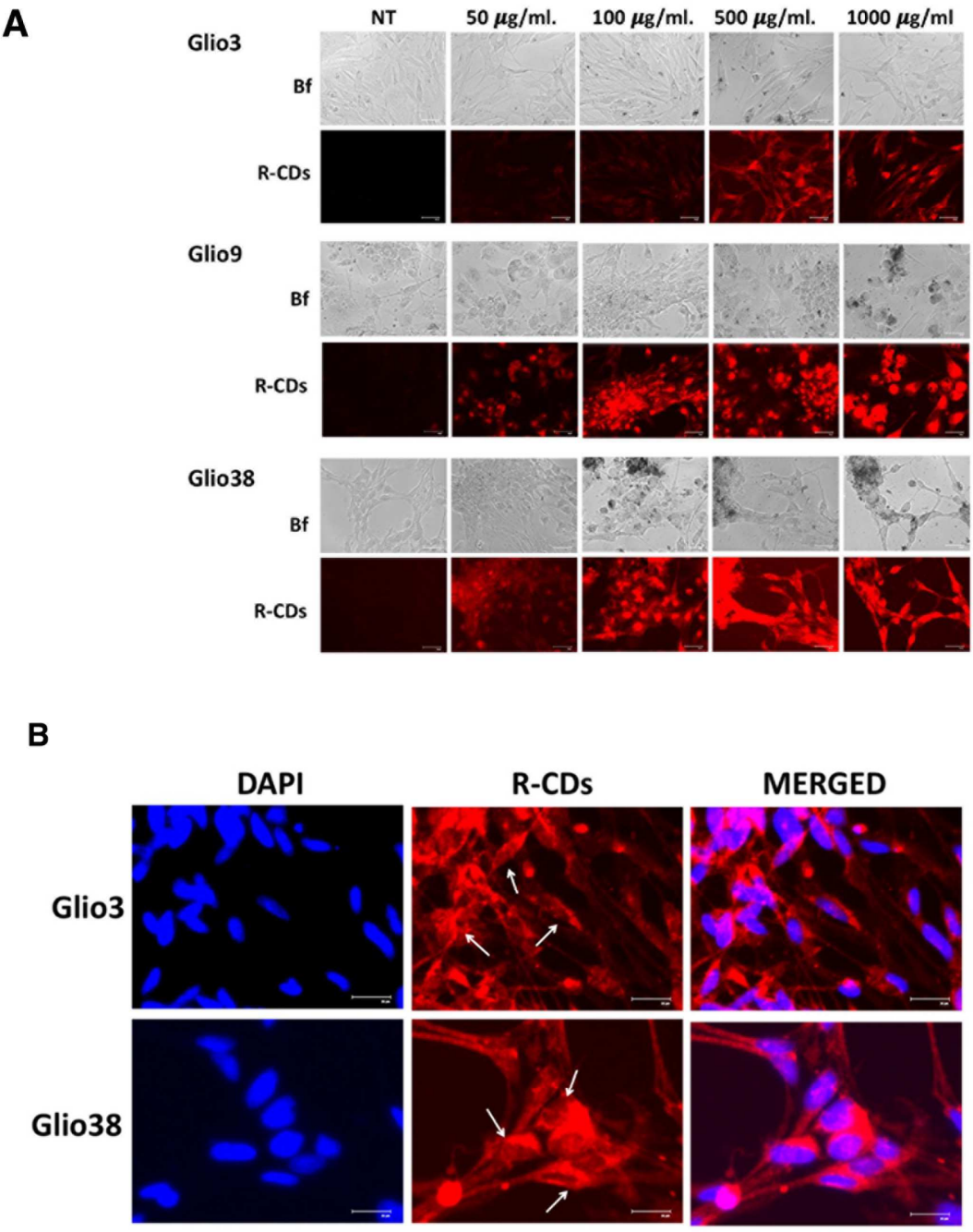

Figure 11. (A) GSCs were exposed to R-CDs as concentrations shown for 6 hrs and imaged with Bf and using the red channel. Scale bar is 50 µm. (B) GSCs were exposed to 500 µg/mL for 1 h and the fluorescent intensity observed. DAPI was used to stain the cell nucleus. Arrows indicate reduced fluorescent intensity in cell nucleus. Scale bar is 25 µm.

3.5 Drug Efflux Assessment of R-CDs in Glio3 and Glio38

The R-CDs were assessed for their ability to resist drug efflux by both Glio3 and Glio38 neurospheres (**Figure 12A, 12B**). The neurospheres were exposed to R-CDs for 4 hrs and imaged immediately (0 hr) or at 48 hrs following the removal of the CDs from the cell culture medium. The neurospheres exhibited robust fluorescence both immediately following exposure as well as 48 hrs later despite the removal of the R-CDs from the cell culture media. This indicates that the R-CDs are not readily effluxed from the GBM neurosphere cells. Overall, these favorable results make sense due to the presence of the PEG-linked network of R-CDs. Literature confirms that PEG plays a key role in efflux pump inhibitions as well as PEGylated compounds generally having a high cellular uptake[94,95]. With these results in mind, we sought to develop tumor selective R-CDs which possess low drug efflux.

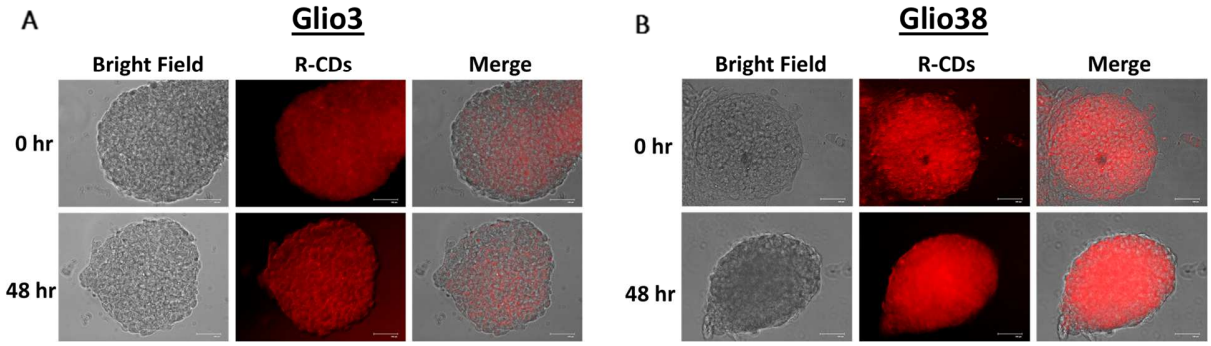

Figure 12. (A) Glio3 and (B) Glio38 neurospheres were treated with 100 ug/ml R-CDs for 4 hrs and imaged immediately (0 hr) for R-CDs removed, neurospheres washed 2 times in cell culture media and incubated an additional 48 hrs prior to

3.7 Cellular Uptake Enhancement by Homing Peptide Conjugation of AKRGARSTA and R-CD

To enhance the cellular uptake of R-CD, the conjugation between the CD and short homing peptide AKRGARSTA was described in the **Experimental Section** with the scheme provided in

Figure 13. This particular peptide is known to provide higher cellular uptake towards GBM cell lines since its mechanism of action relies on the interaction with key cell receptors. Based on our PCR results (**Figure S5-6**), GBM cells overexpress neuropilin1 (NRP1) and p32 (C1QBP) which normally interacts with AKRGASTA peptide for cellular intake. The rationale of why we are interested in this specific homing peptide is due to the fact that there is a significantly higher expression of both neuropilin1 (NRP1) and p32 (C1QBP) in GBM than in the normal brain as provided in **Figure S5-6**. Furthermore, the justification of this reaction stems from AKRGARSTA peptide's mode of action regarding GBM. The initial interaction of AKRGARSTA begins at the p32 receptor of GBM tumor cells which are overexpressed on the surface of vascular and malignant cells followed by proteolytic processing. This process then exposes the C-end Rule (CendR) motif of the peptide (AKRGAR) to enable neuropilin-1 (NRP-1) binding[96]. Thus, activating a specialized tumor penetration pathway. AKRGARSTA has been established as a conjugate for nanoparticles to deliver targeted treatment of breast cancer and glioblastoma[97,98]. Therefore, we posit that through this conjugation, the R-CD conjugates will effectively enhance cellular uptake as provided in **Figure 14**.

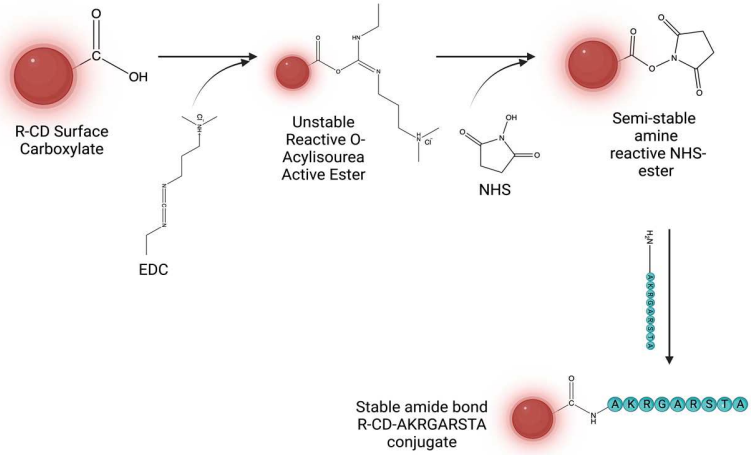

Figure 13. Schematic representation of the conjugation of AKRGARSTA to R-CD (R-CD-AKRGARSTA) using

552

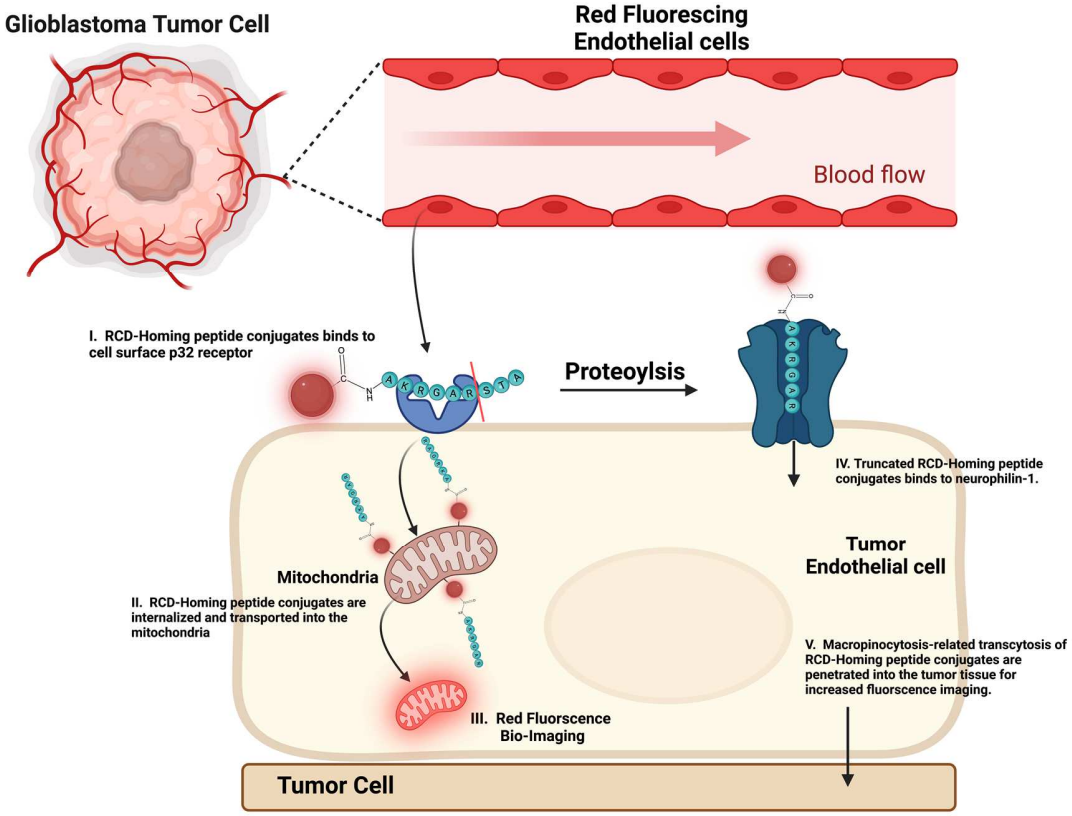

Figure 14. Schematic representation of the R-CD-AKRGARSTA penetration pathway with GBM. Created with BioRender.com

553

Regarding the characterization of the conjugate to ensure the success of the reaction, CDS was implemented to detect the presence of the peptide on the purified product. CDS is one of the main techniques used to determine the secondary structure of a protein or peptide, making it possible to obtain its ellipticity signal[99,100]. A protein's structure mainly depends on the amino acid sequence and its length. The longer the peptide chain, the more complex the structure can be. Furthermore, the amino acid within the peptide tends to intramolecularly interact with one another via dipole-dipole (H-bonding), π-related and hydrophobic interactions, alongside covalent bond as disulfide bridges between cysteine residues[101,102]. In addition to these interactions, solvents also influence the final structure of the proteins which dictates their functionality according to their stabilization[103]. Therefore, investigation of its architecture is a must to understand how it interacts and behaves with other compounds. When proteins or peptides are studied using CDS, it is possible to obtain insights about their structure[104,105].Based on the implementation of this methodology to our system, the data displayed on **Figure 15A** indicates that the R-CDs do not present any significant signal on the CDS which concludes that R-CDs are identified as non-chiral nanoparticles. In contrast, when the conjugated sample (R-CD-AKRGARSTA) was analyzed, the ellipticity signal within the range of 190 – 250 nm suggests that the coupling reaction was successful. Due to the small number of amino acids residues (9), the peptide cannot form a more complex structure than a random coil based on comparisons with the literature. In addition, to further sustain the random coil as the structure of this peptide, we utilized the Beta Structure Selection (BeStSel) algorithm on the CDS spectrum which didn't present any predominant beta-sheet structure (80 % or higher) as shown in **Figure 15B**[106–108].

A

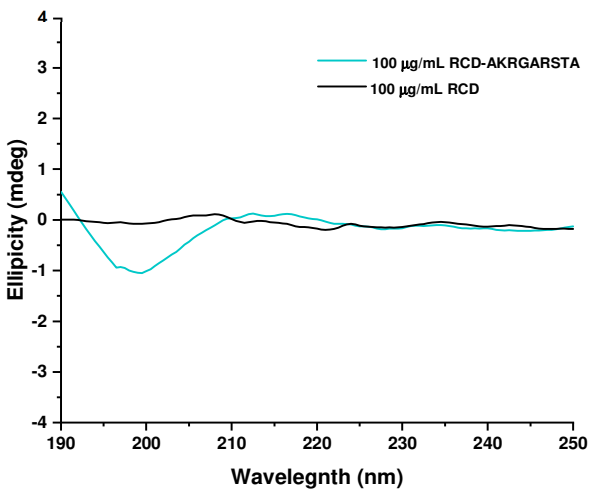

B

Estimated Secondary Structure content	%
Helix	0
Antiparallel	42
Parallel	0
Turn	15
Others	43

Figure 15. (A) Circular Dichroism spectra of naked R-CD and R-CD conjugated to AKRGARSTA; (B) BeStSel estimated secondary structure based on the circular dichroism data. The analysis of the BeStSel was repeated three times for each CD with an experimental uncertainty of $\mp$ 0.10%.

576

577 To assess the discreet differences of cellular uptake between cell lines, Glio3, Glio9, Glio38
578 and non-cancer MSCs were treated with 100 µM of either R-CD or R-CD peptide conjugate for
579 1 hr and evaluated by fluorescent microscopy (**Figure 16**). Non-treated (NT) cells were included
580 as a control. Remarkedly, the images show a vast difference in fluorescence intensity between
581 both R-CD and R-CD-AKRGARSTA. Although the red channel imaging of R-CD is favorable,
582 clearly the conjugate boasts superiority in terms of imaging capabilities for Glio3, Glio9, and
583 Glio38. We can ascribe this result due to the enhanced selectivity of tumor cells over non-tumor
584 cells via the short homing peptide AKRGARSTA as described previously. This specificity is
585 evident when observing the red channel of the non-tumor MSC cell line as there are less
586 significant changes between the CDs and conjugate.

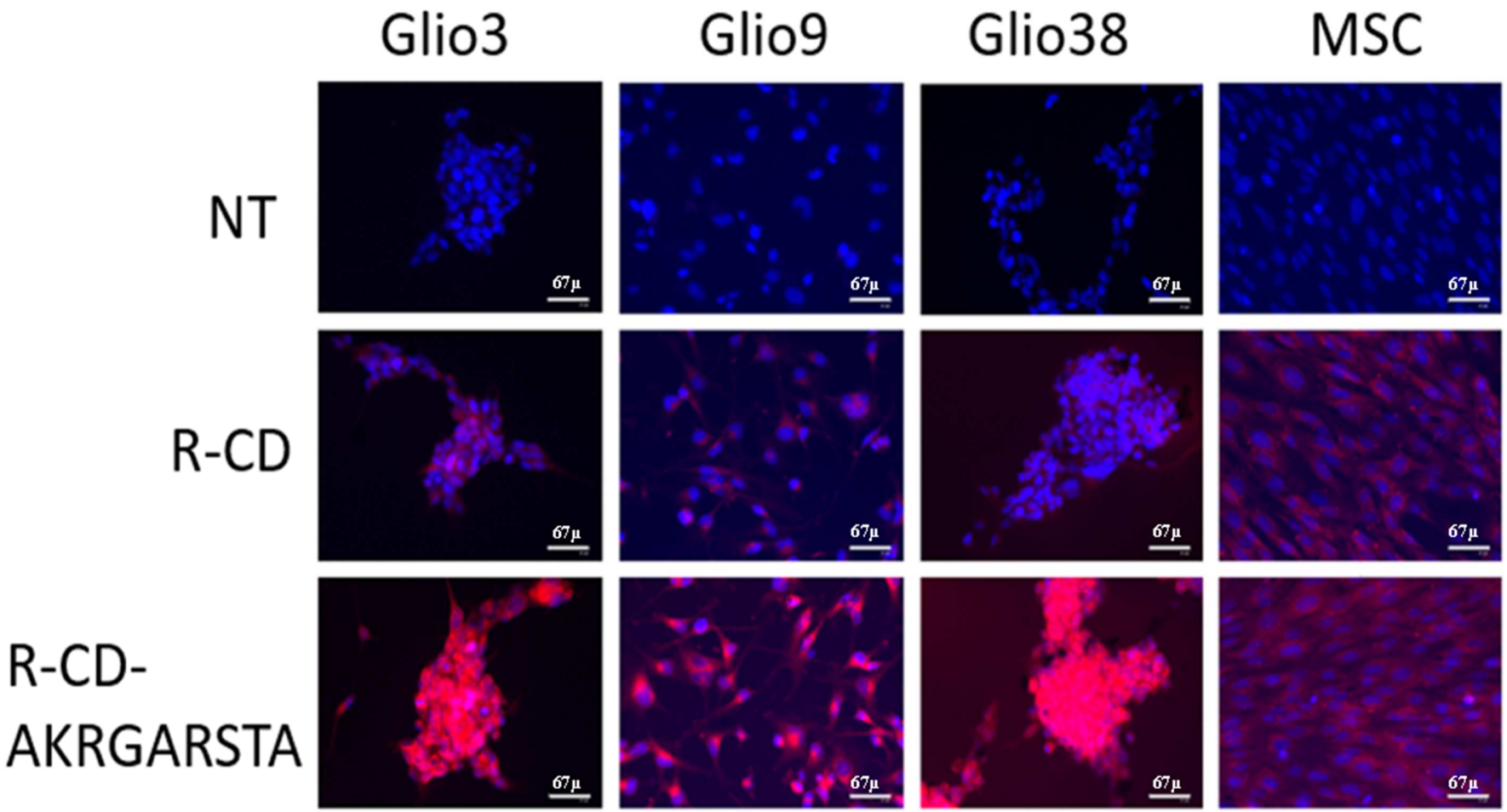

Figure 16. Effect of peptide targeting of R-CDs on cell cancer and non-cancer cells. A. GSC lines Glio3, Glio9, Glio38 and non-cancer MSCs were treated with 100 µM of either R-CDs or R-CD- peptide conjugate (Conjugate) for 1 hr and evaluated by fluorescent microscopy. Non-treated (NT) cells were included as a control. Cell nuclei were stained with DAPI (blue channel) and CD fluorescence. Scale bar represents 67 microns and was visualized using the red channel. Merged red and blue channels are shown.

588 To elucidate the degree of fluorescent enhancement between the CD and its conjugate, both
589 mean fluorescence intensity and percent increase of corrected total cell fluorescence (CTCF)
590 were determined as described in **Experimental Section**. The observation of the mean
591 fluorescence in both GSC and MSCs are again noted to have noticeable differences which
592 correspond to nanoparticle uptake between the CD and CD conjugate (**Figure 17A**). With
593 regards to the results on R-CDs, whereas the mean fluorescence in MSC is 64, in Glio3, Glio9,
594 and Glio38 the values are 61, 39 and 66, respectively. Yet to our satisfaction, R-CD-
595 AKRGARSTA yielded much higher mean fluorescence with Glio3, Glio9, and Glio38 having
596 values of 156, 87 and 186, respectively. This data not only corroborates the earlier suggestion
597 that the conjugate has an effective mechanism for cellular uptake, but also indicates that there
598 was minimal alteration in the material intake by MSC. The mean fluorescence of conjugated R-
599 CDs in MSC provided a value of 77, which is only slightly higher than that of bare R-CDs. To
600 provide clearer insight into the increase of fluorescence due to the enhancement of cellular
601 uptake of the CDs, the CTCF values between R-CD and R-CD-AKRGARSTA were calculated
602 to determine the percent increase of fluorescence (**Figure 17B**). As expected, the data yielded
603 highly valuable information which supports the qualitative observation of the initial images. In
604 Glio3, Glio9, and Glio38, R-CD-AKRGARSTA has shown to increase the CTCF by 2.56, 2.23,
605 and 2.82-fold, respectively. In MSC, the conjugate only resulted in a CTCF increase of 1.2-fold.
606 The specificity of R-CD-pep for the tumor cells can also be demonstrated in **Figure S7** in which
607 Glio3, Glio9, Glio38 and MSCs were exposed to only 50 μM R-CD-Pep and imaged by
608 fluorescent microscopy. While the GBM stem cell lines, Glio3, Glio9 and Glio38 clearly
609 demonstrated pronounced fluorescence, the fluorescence of the non-tumorous MSCs is barely

610 visibly. These results support our hypothesis that the peptide bound onto the surface of R-CD
611 has specificity to mainly target GBM tumor cells.

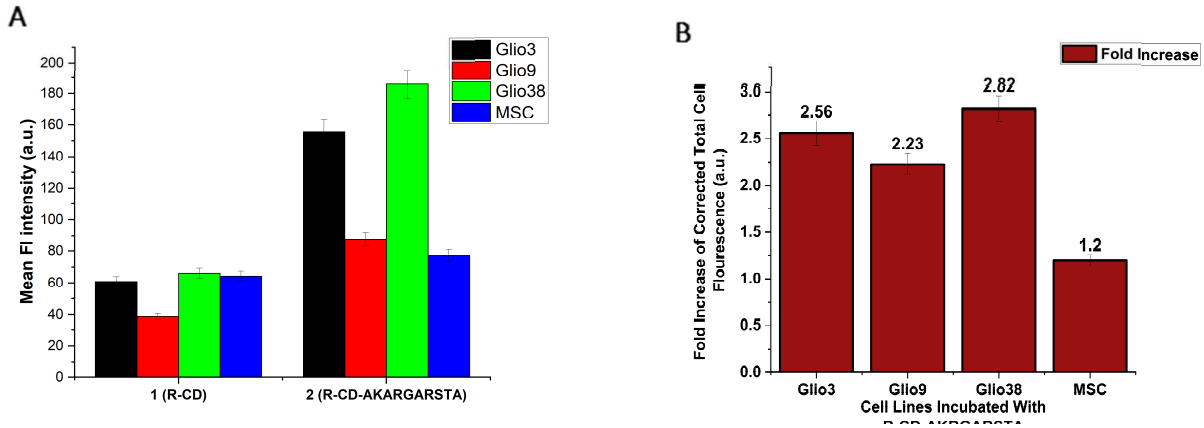

Figure 17. Fluorescence assessment of 100 µM CDs incubated for 1 hr of CDs on GSC cell lines Glio3, Glio9, Glio38 and non-cancer MSC. (A) Mean fluorescence intensity. (B) Fold increase of CTCF from R-CD-AKRGARSTA when compared to R-CD.

612

613 *3.7 Crossing the BBB via R-CD-Tf Conjugate in zebrafish model*

614 Given the nature of GBM, it is imperative to address the challenge to cross the BBB. To be
615 specific, the CNS comprises of both the brain and spinal cord which is protected by the intricate
616 mechanisms that are regulated within the BBB[34]. Moreso, the BBB serves as a physiological
617 point of entry that has high specificity towards what molecules are permitted entry from the
618 blood circulation of the host into the CNS. This feature coupled with physical characteristics of
619 the BBB being composed of capillary endothelial cells that are interconnected by tight junctions
620 leads to the difficult transport of materials such as drugs or CDs into the CNS[109]. In fact, the vast
621 majority of both large molecules and nanoparticles are unable to pass the BBB without surface
622 modifications[110]. To remedy this limitation, our group has successfully conjugated R-CDs (R-
623 CD-Tf) with the ligand transferrin with a scheme provided in **Figure 18A**. Transferrin was

selected as the ligand of choice due to the BBB's brain capillary endothelial cells having a high degree of expressed transferrin receptors. These transferrin receptors have been proven to permit the entrance of transferrin-conjugated nanoparticles according to literature[111].

To investigate the prospect of transporting R-CD-Tf into the CNS the zebra model was due to their physiological homology to humans. This complex vertebrae species possesses the ideal hormones, receptors, and major neurotransmitters that allow researchers to develop therapeutic agents *in vivo* that can be extended to human disease[112]. Furthermore, given their physical attributes such as small size, transparent body, and conditions to breed, the zebrafish is a more facile model to both simulate and follow non-invasive imaging techniques in the CNS than that of mice[113]. The larval zebra fish were used at 5 days post fertilization as studies conclude that the maturation of the BBB of zebrafish is completed within 3 days comparable to mammals[114]. As indicated in **Figure 18B**, the CDs of choice were injected into the heart of the larval zebrafish to allow the pumping of the material through the blood stream. We predict that, in comparison to R-CD, R-CD-Tf will successfully be received by the transferrin receptor and transported through the BBB and into the CNS.

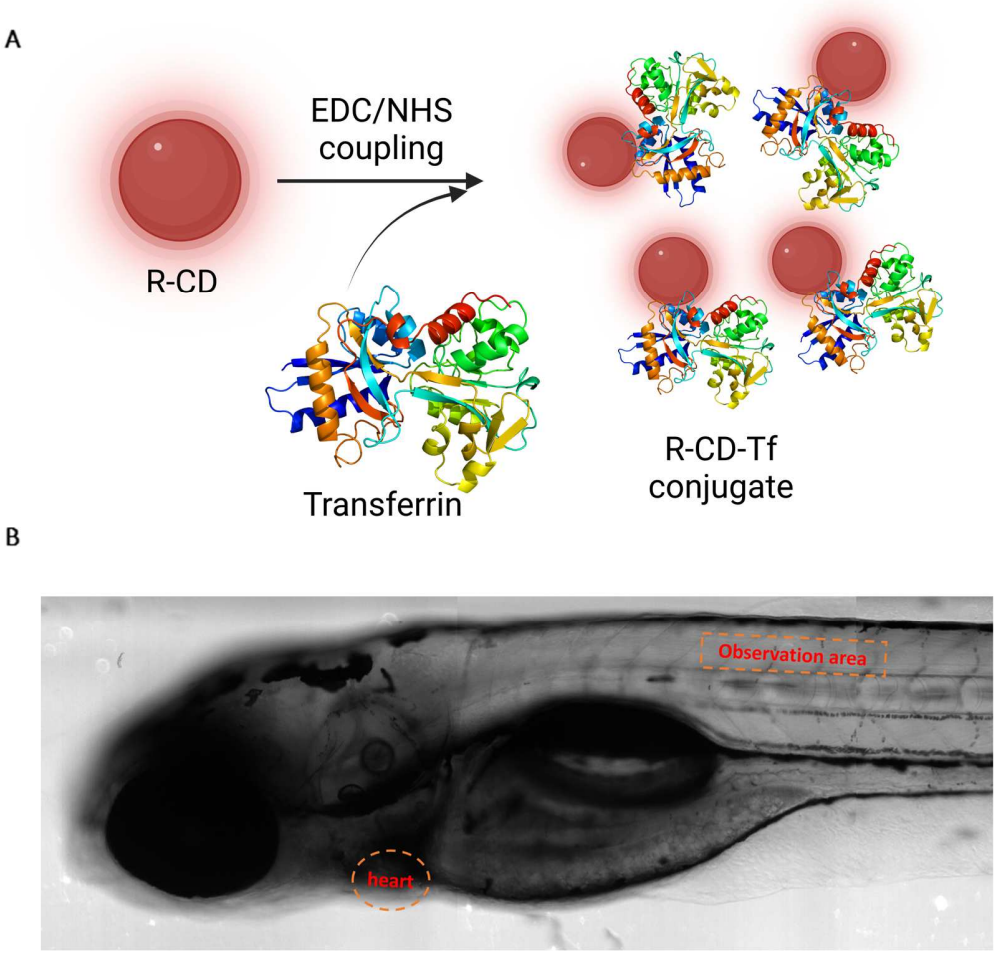

Figure 18. (A) Schematic representation of the conjugation of transferrin to R-CD (R-CD-Tf). (B) Image of zebrafish with the highlighting of both the heart (injection site) and central canal (observation area).

The confocal images of the larval zebrafish were overlapped with the bright field images which yielded quite interesting results (**Figure 19**). As expected, due to the absence of transferrin on the surface, the R-CDs when visualized under 405 nm excitation did not appear to be in the central canal suggesting that the R-CDs did not penetrate the BBB. Although it is worthwhile to note that the R-CDs were able to be clearly observed throughout the image. Upon analysis of the overlapped images containing R-CD-Tf, red fluorescence of the central canal was observed

indicating crossing of the BBB by R-CD-Tf. In following, we hypothesize that the R-CD-Tf were successfully transported into the CNS across the BBB as provided in **Figure 20**. The finding of this result has strong impact in the field of imaging as this is the first time to our knowledge to observe stable, water-soluble and far-red emitting CDs to cross the BBB successfully.

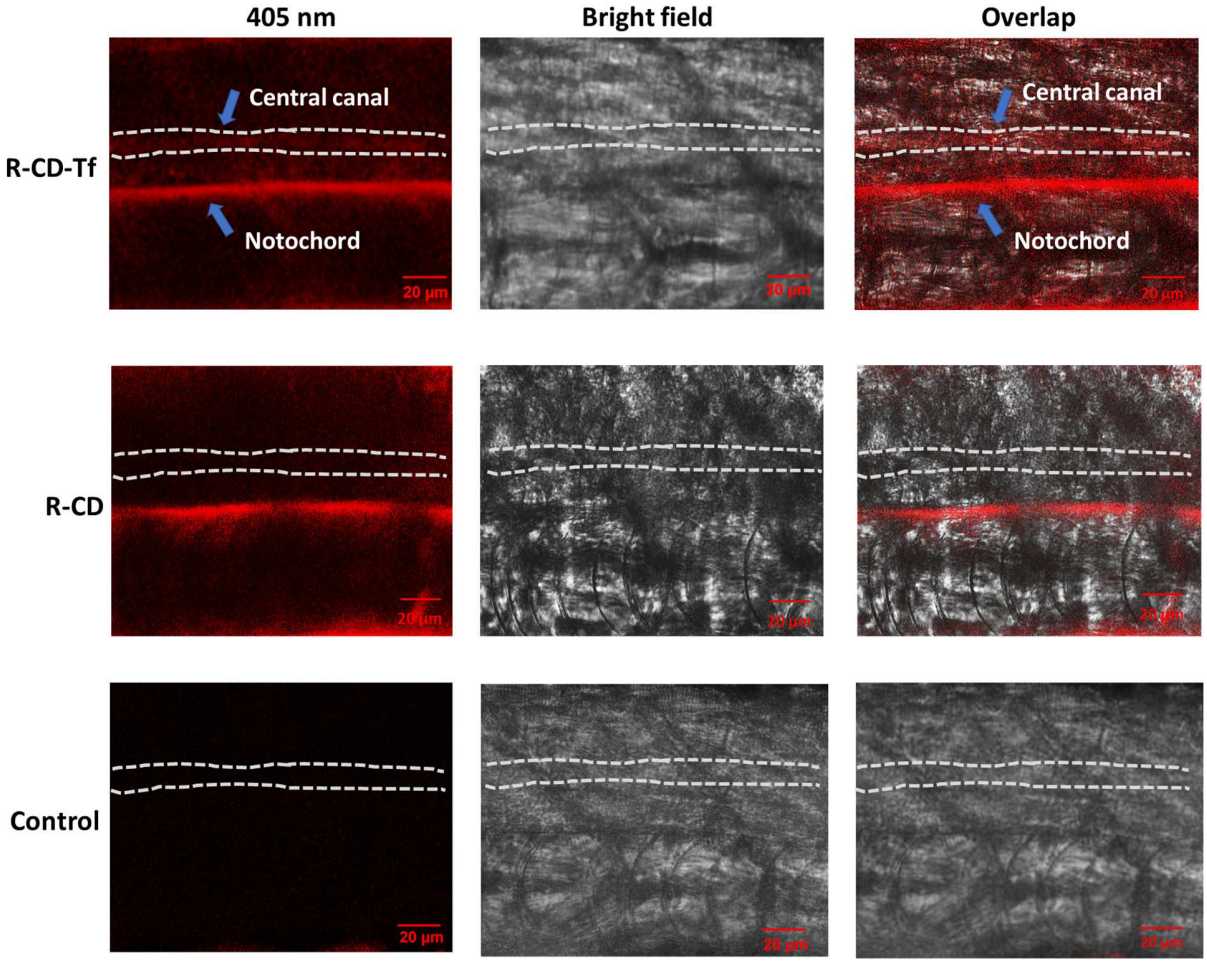

Figure 19. Confocal image of R-CD-Tf versus R-CDs in the CNS of zebrafish under 405 nm excitation. The blue arrow indicates the central canal of spiral cord of zebrafish.

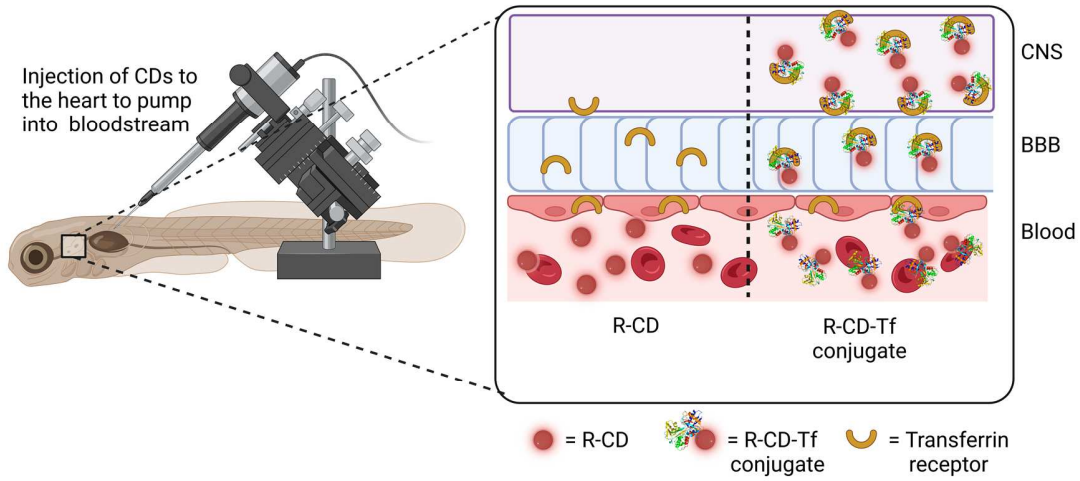

Figure 20. Graphic visualization of the transit of R-CD-Tf via the BBB into the CNS as compared to R-CD in zebrafish. Created with BioRender.com

4. Conclusion

For the first time, we have synthesized a new type of red-emitting CDs derived from mixture of the organic fluorophore ICG, citric acid, and PEG. Ultimately, the red emission was attributed due to the decrease of conjugation of the fluorophore that passivates the CD. Additionally, this is the first report of far-red emission CDs whose applications are favorable in water leading to excellent biocompatibility in comparison to previous reports[115,116]. This type of CD was proven to exhibit low toxicity in both GBM and MSCs and was showcased as suitable materials for enhanced fluorescent imaging of cancer cells including GSCs. Furthermore, post-conjugation we were able to both selectively increase the cellular uptake of CDs into GSC as well as cross the BBB in the zebrafish model. To our knowledge, the this is the first account of CDs bound with AKRGARSTA to increase tumor selectivity. In

664 further application, we believe the potential of both drug delivery and drug tracking is the
665 next step field of study for these types of CDs in the field of theranostics[117,118].

666 **Credit authorship contribution statement**

667 **Justin Domena:** Conceptualization, Methodology, Validation, Formal Analysis, Investigation,
668 Writing- original draft, Writing- review & editing, Project administration.

669 **Braulio C.L.B. Ferreira:** Formal analysis, Methodology, Writing-review & editing.

670 **Emel K. Cilingir:** Methodology, Formal analysis

671 **Yiqun Zhou:** Methodology, Formal analysis, Writing-review & editing

672 **Jiuyan Chen:** Methodology, Formal analysis

673 **Qiaxian R. Johnson:** Formal analysis.

674 **Bhanu P.S. Chauhan:** Formal analysis

675 **Mattia. Bartoli:** Methodology, Formal analysis, Writing-review & editing

676 **Alberto Tagliaferro:** Methodology, Formal analysis, Writing-review & editing

677 **Steven Vanni:** Methodology, Formal analysis

678 **Regina M. Graham:** Methodology, Validation, Formal Analysis, Investigation, Writing-
679 original draft, Writing- review & editing.

680 **Roger M. Leblanc:** Conceptualization, Methodology, Validation, Writing-review & editing.

681 **Declaration of Competing Interest**

682 The authors declare that they have no known competing financial interests or personal
683 relationships that could have appeared to influence the work reported in this paper.

684 **Acknowledgements**

685 Professor Roger Leblanc thanks the support of the National Science Foundation under the
686 grants 1809060 and 2041413. Also, authors gratefully acknowledge the great support from
687 University of Miami, United States.

688 **References**

689 (1) Gunaydin, G.; Gedik, M. E.; Ayan, S. Photodynamic Therapy—Current Limitations and
690 Novel Approaches. *Frontiers in Chemistry*. **2021**, 1–29.
691 https://doi.org/10.3389/fchem.2021.691697.

692 (2) Mourant, J. R.; Canpolat, M.; Brocker, C.; Esponda-Ramos, O.; Johnson, T. M.;
693 Matanock, A.; Stetter, K.; Freyer, J. P. Light Scattering from Cells: The Contribution of
694 the Nucleus and the Effects of Proliferative Status. *https://doi.org/10.1117/1.429979* **2000**,
695 *5* (2), 131–137. https://doi.org/10.1117/1.429979.

696 (3) François, A.; Marchal, S.; Guillemin, F.; Bezdetnaya, L. MTHPC-Based Photodynamic
697 Therapy Induction of Autophagy and Apoptosis in Cultured Cells in Relation to
698 Mitochondria and Endoplasmic Reticulum Stress. *Int. J. Oncol.* **2011**, *39* (6), 1537–1543.
699 https://doi.org/10.3892/IJO.2011.1174/HTML.

700 (4) van Straten, D.; Mashayekhi, V.; de Bruijn, H. S.; Oliveira, S.; Robinson, D. J. Oncologic
701 Photodynamic Therapy: Basic Principles, Current Clinical Status and Future Directions.
702 *Cancers*. **2017**, 1–54. https://doi.org/10.3390/cancers9020019.

703 (5) Abrahamse, H.; Hamblin, M. R. New Photosensitizers for Photodynamic Therapy.
704 *Biochem. J.* **2016**, *473* (4), 347–364. https://doi.org/10.1042/BJ20150942.

705 (6) Zhao, X.; Liu, J.; Fan, J.; Chao, H.; Peng, X. Recent Progress in Photosensitizers for
706 Overcoming the Challenges of Photodynamic Therapy: From Molecular Design to

Application. *Chemical Society Reviews*. **2021**, 4185–4219. https://doi.org/10.1039/d0cs00173b.

(7) Allison, R. R.; Downie, G. H.; Cuenca, R.; Hu, X. H.; Childs, C. J. H.; Sibata, C. H. Photosensitizers in Clinical PDT. *Photodiagnosis Photodyn. Ther.* **2004**, *1* (1), 27–42. https://doi.org/10.1016/S1572-1000(04)00007-9.

(8) Park, J.; Lee, Y. K.; Park, I. K.; Hwang, S. R. Current Limitations and Recent Progress in Nanomedicine for Clinically Available Photodynamic Therapy. *Biomedicines* **2021**, *9* (1), 1–17. https://doi.org/10.3390/BIOMEDICINES9010085.

(9) Zeng, Q.; Shao, D.; He, X.; Ren, Z.; Ji, W.; Shan, C.; Qu, S.; Li, J.; Chen, L.; Li, Q. Carbon Dots as a Trackable Drug Delivery Carrier for Localized Cancer Therapy in Vivo. *J. Mater. Chem. B* **2016**, *4* (30), 5119–5126. https://doi.org/10.1039/C6TB01259K.

(10) Wang, L.; Pan, H.; Gu, D.; Li, P.; Su, Y.; Pan, W. A Composite System Combining Self-Targeted Carbon Dots and Thermosensitive Hydrogels for Challenging Ocular Drug Delivery. *J. Pharm. Sci.* **2022**, *111* (5), 1391–1400. https://doi.org/10.1016/J.XPHS.2021.09.026.

(11) Zhang, W.; Kandel, N.; Zhou, Y.; Smith, N.; C.L.B. Ferreira, B.; Perez, M.; Claure, M. L.; Mintz, K. J.; Wang, C.; Leblanc, R. M. Drug Delivery of Memantine with Carbon Dots for Alzheimer's Disease: Blood–Brain Barrier Penetration and Inhibition of Tau Aggregation. *J. Colloid Interface Sci.* **2022**, *617*, 20–31. https://doi.org/10.1016/j.jcis.2022.02.124.

(12) Wang, F. T.; Wang, L. N.; Xu, J.; Huang, K. J.; Wu, X. Synthesis and Modification of Carbon Dots for Advanced Biosensing Application. *Analyst* **2021**, *146* (14), 4418–4435. https://doi.org/10.1039/D1AN00466B.

(13) Ji, C.; Zhou, Y.; Leblanc, R. M.; Peng, Z. Recent Developments of Carbon Dots in Biosensing: A Review. *ACS Sensors* **2020**, *5* (9), 2724–2741. https://doi.org/10.1021/ACSSENSORS.0C01556.

(14) Yang, S. T.; Cao, L.; Luo, P. G.; Lu, F.; Wang, X.; Wang, H.; Meziani, M. J.; Liu, Y.; Qi,

G.; Sun, Y. P. Carbon Dots for Optical Imaging in Vivo. *J. Am. Chem. Soc.* **2009**, *131* (32), 11308–11309. https://doi.org/10.1021/JA904843X.

(15) Zhu, A.; Qu, Q.; Shao, X.; Kong, B.; Tian, Y. Carbon-Dot-Based Dual-Emission Nanohybrid Produces a Ratiometric Fluorescent Sensor for In Vivo Imaging of Cellular Copper Ions. *Angew. Chemie* **2012**, *124* (29), 7297–7301. https://doi.org/10.1002/ANGE.201109089.

(16) Chandra, A.; Singh, N. Biocompatible Fluorescent Carbon Dots for Ratiometric Intracellular PH Sensing. *ChemistrySelect* **2017**, *2* (20), 5723–5728. https://doi.org/10.1002/SLCT.201701012.

(17) Zhu, A.; Qu, Q.; Shao, X.; Kong, B.; Tian, Y. Carbon-Dot-Based Dual-Emission Nanohybrid Produces a Ratiometric Fluorescent Sensor for In Vivo Imaging of Cellular Copper Ions. *Angew. Chemie Int. Ed.* **2012**, *51* (29), 7185–7189. https://doi.org/10.1002/ANIE.201109089.

(18) Zaidi, F.; Rais, A.; Chand, P.; Malik, M.; Kulanthaivel, S.; Mishra, P.; Prasad, T. Non-Toxic L-Phenylalanine Doped Carbon Dots: High Performance Photoluminescent Agent for Bioimaging. *ECS Trans.* **2022**, *107* (1), 8329–8338. https://doi.org/10.1149/10701.8329ecst.

(19) Hu, Y.; Yang, Z.; Chen, G.; Hao, X.; Bian, J.; Peng, F. Strong and Highly Conductive Poly(Vinyl Alcohol)/Carbon Dot/EGaIn Composite Films for Flexible and Transient Electronics. *ACS Appl. Polym. Mater.* **2022**, *2022*, 3655. https://doi.org/10.1021/acsapm.2c00191.

(20) Wang, X.; Chen, S.; Ma, Y.; Zhang, T.; Zhao, Y.; He, T.; Huang, H.; Zhang, S.; Rong, J.; Shi, C.; Tang, K.; Liu, Y.; Kang, Z. Continuous Homogeneous Catalytic Oxidation of C–H Bonds by Metal-Free Carbon Dots with a Poly(Ascorbic Acid) Structure. *ACS Appl. Mater. Interfaces* **2022**, *14* (23), 26682–26689. https://doi.org/10.1021/acsami.2c03627.

(21) Luo, Q.; He, S.; Huang, Y.; Lei, Z.; Qiao, J.; Li, Q.; Xu, D.; Guo, X.; Wu, Y. Non-Toxic Fluorescent Molecularly Imprinted Hydrogel Based on Wood-Derived Cellulose

Nanocrystals and Carbon Dots for Efficient Sorption and Sensitive Detection of Tetracycline. *Ind. Crops Prod.* **2022**, *177*, 114528. https://doi.org/10.1016/j.indcrop.2022.114528.

(22) Feng, Y.; Li, R.; Zhou, P.; Duan, C. Non-Toxic Carbon Dots Fluorescence Sensor Based on Chitosan for Sensitive and Selective Detection of Cr (VI) in Water. *Microchem. J.* **2022**, *180*, 107627. https://doi.org/10.1016/j.microc.2022.107627.

(23) Zhang, S.; Fan, X.; Guan, R.; Hu, Y.; Jiang, S.; Shao, X.; Wang, S.; Yue, Q. Carbon Dots as Metal-Free Photocatalyst for Dye Degradation with High Efficiency within Nine Minutes in Dark. *Opt. Mater. (Amst).* **2022**, *123*, 111914. https://doi.org/10.1016/j.optmat.2021.111914.

(24) Xu, L.; Tu, H.; Zhu, F.; Xiang, Y.; Luo, Z.; Fang, S.; Deng, W.; Zou, G.; Hou, H.; Ji, X. Carbon Dots for Ultrastable Solid-state Batteries. *SmartMat* **2022**. https://doi.org/10.1002/smm2.1097.

(25) Mary, S. K.; Koshy, R. R.; Arunima, R.; Thomas, S.; Pothen, L. A. A Review of Recent Advances in Starch-Based Materials: Bionanocomposites, PH Sensitive Films, Aerogels and Carbon Dots. *Carbohydrate Polymer Technologies and Applications*. Elsevier June 1, **2022**, 100190. https://doi.org/10.1016/j.carpta.2022.100190.

(26) Jiang, Y.; Ji, C.; Wu, J.; Han, Q.; Cui, C.; Shi, W.; Peng, Z. Formation, Photoluminescence and in Vitro Bioimaging of Polyethylene Glycol-Derived Carbon Dots: The Molecular Weight Effects. *Polymer (Guildf).* **2022**, *243*, 124625. https://doi.org/10.1016/j.polymer.2022.124625.

(27) Meng, Y.; Zhang, Z.; Zhao, H.; Jiao, Y.; Li, J.; Shuang, S.; Dong, C. Facile Synthesis of Multifunctional Carbon Dots with 54.4% Orange Emission for Label-Free Detection of Morin and Endogenous/Exogenous Hypochlorite. *J. Hazard. Mater.* **2022**, *424*, 127289. https://doi.org/10.1016/j.jhazmat.2021.127289.

(28) Da, X.; Han, Z.; Yang, Z.; Zhang, D.; Hong, R.; Tao, C.; Lin, H.; Huang, Y. Preparation of Multicolor Carbon Dots with High Fluorescence Quantum Yield and Application in

White LED. *Chem. Phys. Lett.* **2022**, *794*, 139497. https://doi.org/10.1016/j.cplett.2022.139497.

(29) Susu Zhang; Li Yuan; Guozheng Liang; Aijuan Gu. Preparation of Multicolor-Emissive Carbon Dots with High Quantum Yields and Their Epoxy Composites for Fluorescence Anti-Counterfeiting and Light-Emitting Devices. *J. Mater. Chem. C* **2022**, *10* (21), 8441–8458. https://doi.org/10.1039/D2TC00789D.

(30) Ding, H.; Yu, S. B.; Wei, J. S.; Xiong, H. M. Full-Color Light-Emitting Carbon Dots with a Surface-State-Controlled Luminescence Mechanism. *ACS Nano* **2016**, *10* (1), 484–491. https://doi.org/10.1021/ACSNANO.5B05406.

(31) Zheng, M.; Li, Y.; Liu, S.; Wang, W.; Xie, Z.; Jing, X. One-Pot to Synthesize Multifunctional Carbon Dots for Near Infrared Fluorescence Imaging and Photothermal Cancer Therapy. *ACS Appl. Mater. Interfaces* **2016**, *8* (36), 23533–23541. https://doi.org/10.1021/ACSAMI.6B07453.

(32) Burri, S. H.; Gondi, V.; Brown, P. D.; Mehta, M. P. The Evolving Role of Tumor Treating Fields in Managing Glioblastoma: Guide for Oncologists. *Am. J. Clin. Oncol. Cancer Clin. Trials* **2018**, *41* (2), 191–196. https://doi.org/10.1097/COC.0000000000000395.

(33) Kamiya-Matsuoka, C.; Gilbert, M. R. Treating Recurrent Glioblastoma: An Update. *CNS Oncol.* **2015**, *4* (2), 91–104. https://doi.org/10.2217/cns.14.55.

(34) Davis, M. E. Glioblastoma: Overview of Disease and Treatment. *Clin. J. Oncol. Nurs.* **2016**, *20* (5), 1–8. https://doi.org/10.1188/16.CJON.S1.2-8.

(35) Auffinger, B.; Spencer, D.; Pytel, P.; Ahmed, A. U.; Lesniak, M. S. The Role of Glioma Stem Cells in Chemotherapy Resistance and Glioblastoma Multiforme Recurrence. *Expert Rev. Neurother.* **2015**, *15* (7), 741–752. https://doi.org/10.1586/14737175.2015.1051968.

(36) Tang, X.; Zuo, C.; Fang, P.; Liu, G.; Qiu, Y.; Huang, Y.; Tang, R. Targeting Glioblastoma Stem Cells: A Review on Biomarkers, Signal Pathways and Targeted Therapy. *Frontiers in Oncology*. **2021**, 2703-2711. https://doi.org/10.3389/fonc.2021.701291.

(37) Lathia, J. D.; Mack, S. C.; Mulkearns-Hubert, E. E.; Valentim, C. L. L.; Rich, J. N. Cancer Stem Cells in Glioblastoma. *Genes Dev* **2015**, *29* (12), 1203–1217. https://doi.org/10.1101/gad.261982.115.

(38) Alves, A. L. V.; Gomes, I. N. F.; Carloni, A. C.; Rosa, M. N.; da Silva, L. S.; Evangelista, A. F.; Reis, R. M.; Silva, V. A. O. Role of Glioblastoma Stem Cells in Cancer Therapeutic Resistance: A Perspective on Antineoplastic Agents from Natural Sources and Chemical Derivatives. *Stem Cell Res. Ther. 2021 121* **2021**, *12* (1), 1–22. https://doi.org/10.1186/S13287-021-02231-X.

(39) Jackson, C. M.; Choi, J.; Lim, M. Mechanisms of Immunotherapy Resistance: Lessons from Glioblastoma. *Nat. Immunol.* **2019**, *20* (9), 1100–1109. https://doi.org/10.1038/s41590-019-0433-y.

(40) Wang, Z.; Zhang, H.; Xu, S.; Liu, Z.; Cheng, Q. The Adaptive Transition of Glioblastoma Stem Cells and Its Implications on Treatments. *Signal Transduct. Target. Ther. 2021 61* **2021**, *6* (1), 1–13. https://doi.org/10.1038/s41392-021-00491-w.

(41) Wykes, V.; Zisakis, A.; Irimia, M.; Ughratdar, I.; Sawlani, V.; Watts, C. Importance and Evidence of Extent of Resection in Glioblastoma. *Journal of Neurological Surgery, Part A: Central European Neurosurgery*. **2021**, 75–86. https://doi.org/10.1055/s-0040-1701635.

(42) Teixidor, P.; Arraez, M. A.; Villalba, G.; Garcia, R.; Tardaguila, M.; Gonzalez, J. J.; Rimbau, J.; Vidal, X.; Montane, E. Safety and Efficacy of 5-Aminolevulinic Acid for High Grade Glioma in Usual Clinical Practice: A Prospective Cohort Study. *PLoS One* **2016**, *11* (2). https://doi.org/10.1371/journal.pone.0149244.

(43) Lau, D.; Hervey-Jumper, S. L.; Chang, S.; Molinaro, A. M.; McDermott, M. W.; Phillips, J. J.; Berger, M. S. A Prospective Phase II Clinical Trial of 5-Aminolevulinic Acid to Assess the Correlation of Intraoperative Fluorescence Intensity and Degree of Histologic Cellularity during Resection of High-Grade Gliomas. *J. Neurosurg.* **2016**, *124* (5), 1300–1309. https://doi.org/10.3171/2015.5.JNS1577.

(44) Valdes, P. A.; Juvekar, P.; Agar, N. Y. R.; Gioux, S.; Golby, A. J. Quantitative Wide-Field Imaging Techniques for Fluorescence Guided Neurosurgery. *Frontiers in Surgery*. **2019**, 1-18. https://doi.org/10.3389/fsurg.2019.00031.

(45) Tu, L.; Luo, Z.; Wu, Y. L.; Huo, S.; Liang, X. J. Gold-Based Nanomaterials for the Treatment of Brain Cancer. *Cancer Biol. Med.* **2021**, *18* (2), 372. https://doi.org/10.20892/J.ISSN.2095-3941.2020.0524.

(46) Zhao, W.; Yu, X.; Peng, S.; Luo, Y.; Li, J.; Lu, L. Construction of Nanomaterials as Contrast Agents or Probes for Glioma Imaging. *J. Nanobiotechnology* **2021**, *19* (1), 1–31. https://doi.org/10.1186/S12951-021-00866-9.

(47) Karim, R.; Palazzo, C.; Evrard, B.; Piel, G. Nanocarriers for the Treatment of Glioblastoma Multiforme: Current State-of-the-Art. *J. Control. Release* **2016**, *227*, 23–37. https://doi.org/10.1016/J.JCONREL.2016.02.026.

(48) Porcu, E. P.; Salis, A.; Gavini, E.; Rassu, G.; Maestri, M.; Giunchedi, P. Indocyanine Green Delivery Systems for Tumour Detection and Treatments. *Biotechnol. Adv.* **2016**, *34* (5), 768–789. https://doi.org/10.1016/J.BIOTECHADV.2016.04.001.

(49) Dai, Q.; Ren, E.; Xu, D.; Zeng, Y.; Chen, C.; Liu, G. Indocyanine Green-Based Nanodrugs: A Portfolio Strategy for Precision Medicine. *Prog. Nat. Sci. Mater. Int.* **2020**, *30* (5), 577–588. https://doi.org/10.1016/J.PNSC.2020.08.002.

(50) Alander, J. T.; Kaartinen, I.; Laakso, A.; Pätilä, T.; Spillmann, T.; Tuchin, V. V.; Venermo, M.; Välisuo, P. A Review of Indocyanine Green Fluorescent Imaging in Surgery. *International Journal of Biomedical Imaging*. **2012**, 1–26. https://doi.org/10.1155/2012/940585.

(51) Mordon, S.; Devoisselle, J. M.; Soulie-Begu, S.; Desmettre, T. Indocyanine Green: Physicochemical Factors Affecting Its Fluorescence in Vivo. *Microvasc. Res.* **1998**, *55* (2), 146–152. https://doi.org/10.1006/mvre.1998.2068.

(52) Jiang, Y.; Tan, Z.; Zhao, T.; Wu, J.; Li, Y.; Jia, Y.; Peng, Z. Indocyanine Green Derived Carbon Dots with Significantly Enhanced Properties for Efficient Photothermal Therapy.

Nanoscale **2022**, *15* (4), 1925–1936. https://doi.org/10.1039/d2nr06058b.

(53) Sansalone, L.; Veliz, E. A.; Myrthil, N. G.; Stathias, V.; Walters, W.; Torrens, I. I.; Schürer, S. C.; Vanni, S.; Leblanc, R. M.; Graham, R. M. Novel Curcumin Inspired Bis-Chalcone Promotes Endoplasmic Reticulum Stress and Glioblastoma Neurosphere Cell Death. *Cancers (Basel).* **2019**, *11* (3). https://doi.org/10.3390/cancers11030357.

(54) Shah, S. S.; Rodriguez, G. A.; Musick, A.; Walters, W. M.; de Cordoba, N.; Barbarite, E.; Marlow, M. M.; Marples, B.; Prince, J. S.; Komotar, R. J.; Vanni, S.; Graham, R. M. Targeting Glioblastoma Stem Cells with 2-Deoxy-d-Glucose (2-DG) Potentiates Radiation-Induced Unfolded Protein Response (UPR). *Cancers (Basel).* **2019**, *11* (2). https://doi.org/10.3390/cancers11020159.

(55) Gersey, Z. C.; Rodriguez, G. A.; Barbarite, E.; Sanchez, A.; Walters, W. M.; Ohaeto, K. C.; Komotar, R. J.; Graham, R. M. Curcumin Decreases Malignant Characteristics of Glioblastoma Stem Cells via Induction of Reactive Oxygen Species. *BMC Cancer* **2017**, *17* (1). https://doi.org/10.1186/s12885-017-3058-2.

(56) Seven, E. S.; Seven, Y. B.; Zhou, Y.; Poudel-Sharma, S.; Diaz-Rucco, J. J.; Kirbas Cilingir, E.; Mitchell, G. S.; Van Dyken, J. D.; Leblanc, R. M. Crossing the Blood–Brain Barrier with Carbon Dots: Uptake Mechanism and in Vivo Cargo Delivery. *Nanoscale Adv.* **2021**, *3* (13), 3942–3953. https://doi.org/10.1039/d1na00145k.

(57) Lee, B. H.; McKinney, R. L.; Hasan, M. T.; Naumov, A. V. Graphene Quantum Dots as Intracellular Imaging-Based Temperature Sensors. *Materials (Basel).* **2021**, *14* (3), 1–12. https://doi.org/10.3390/ma14030616.

(58) Phan, L. M. T.; Hoang, T. X.; Cho, S. Fluorescent Carbon Dots for Sensitive and Rapid Monitoring of Intracellular Ferrous Ion. *Biosensors* **2022**, *12* (1), 41. https://doi.org/10.3390/bios12010041.

(59) Campbell, E.; Hasan, M. T.; Gonzalez Rodriguez, R.; Akkaraju, G. R.; Naumov, A. V. Doped Graphene Quantum Dots for Intracellular Multicolor Imaging and Cancer Detection. *ACS Biomater. Sci. Eng.* **2019**, *5* (9), 4671–4682.

https://doi.org/10.1021/acsbiomaterials.9b00603.

(60) Arroyave, J. M.; Ambrusi, R. E.; Robein, Y.; Pronsato, M. E.; Brizuela, G.; Di Nezio, M. S.; Centurión, M. E. Carbon Dots Structural Characterization by Solution-State NMR and UV–Visible Spectroscopy and DFT Modeling. *Appl. Surf. Sci.* **2021**, *564*, 150195. https://doi.org/10.1016/j.apsusc.2021.150195.

(61) Petryayeva, E.; Algar, W. R.; Medintz, I. L. Quantum Dots in Bioanalysis: A Review of Applications across Various Platforms for Fluorescence Spectroscopy and Imaging. *Appl. Spectrosc.* **2013**, *67* (3), 215–252. https://doi.org/10.1366/12-06948.

(62) Domena, J. B.; Celebic, E.; Ferreira, B. C. L. B.; Zhou, Y.; Zhang, W.; Chen, J.; Bartoli, M.; Tagliaferro, A.; Johnson, Q.; Chauhan, B. P. S.; Paulino, V.; Olivier, J. H.; Leblanc, R. M. Investigation into Red Emission and Its Applications: Solvatochromic N-Doped Red Emissive Carbon Dots with Solvent Polarity Sensing and Solid-State Fluorescent Nanocomposite Thin Films. *Molecules* **2023**, *28* (4), 1755. https://doi.org/10.3390/molecules28041755.

(63) Mustafa, S.; Devi, V. K.; Pai, R. S. Effect of PEG and Water-Soluble Chitosan Coating on Moxifloxacin-Loaded PLGA Long-Circulating Nanoparticles. *Drug Deliv. Transl. Res.* **2017**, *7* (1), 27–36. https://doi.org/10.1007/s13346-016-0326-7.

(64) Mintz, K. J.; Bartoli, M.; Rovere, M.; Zhou, Y.; Hettiarachchi, S. D.; Paudyal, S.; Chen, J.; Domena, J. B.; Liyanage, P. Y.; Sampson, R.; Khadka, D.; Pandey, R. R.; Huang, S.; Chusuei, C. C.; Tagliaferro, A.; Leblanc, R. M. A Deep Investigation into the Structure of Carbon Dots. *Carbon N. Y.* **2021**, *173*, 433–447. https://doi.org/10.1016/j.carbon.2020.11.017.

(65) Zhou, Y.; Kandel, N.; Bartoli, M.; Serafim, L. F.; ElMetwally, A. E.; Falkenberg, S. M.; Paredes, X. E.; Nelson, C. J.; Smith, N.; Padovano, E.; Zhang, W.; Mintz, K. J.; Ferreira, B. C. L. B.; Cilingir, E. K.; Chen, J.; Shah, S. K.; Prabhakar, R.; Tagliaferro, A.; Wang, C.; Leblanc, R. M. Structure-Activity Relationship of Carbon Nitride Dots in Inhibiting Tau Aggregation. *Carbon N. Y.* **2022**, *193*, 1–16. https://doi.org/10.1016/J.CARBON.2022.03.021.

(66) Zhang, G.; Wen, M.; Wang, S.; Chen, J.; Wang, J. Insights into Thermal Reduction of the Oxidized Graphite from the Electro-Oxidation Processing of Nuclear Graphite Matrix. *RSC Adv.* **2017**, *8* (1), 567–579. https://doi.org/10.1039/C7RA11578D.

(67) Li, J.; Liu, D.; Li, B.; Wang, J.; Han, S.; Liu, L.; Wei, H. A Bio-Inspired Nacre-like Layered Hybrid Structure of Calcium Carbonate under the Control of Carboxyl Graphene. *CrystEngComm* **2015**, *17* (3), 520–525. https://doi.org/10.1039/c4ce01632g.

(68) Li, C.; Ran, Q.; Zhu, R.; Gu, Y. Study on Thermal Degradation Mechanism of a Cured Aldehyde-Functional Benzoxazine. *RSC Adv.* **2015**, *5* (29), 22593–22600. https://doi.org/10.1039/C5RA00350D.

(69) Ravi, N.; Anuar, S. A.; Yusuf, N. Y. M.; Isahak, W. N. R. W.; Masdar, M. S. Amine–Mixed Oxide Hybrid Materials for Carbon Dioxide Adsorption from CO2/H2 Mixture. *Mater. Res. Express* **2018**, *5* (5), 055501. https://doi.org/10.1088/2053-1591/AABF68.

(70) Dai, H.; Gao, X.; Liu, E.; Yang, Y.; Hou, W.; Kang, L.; Fan, J.; Hu, X. Synthesis and Characterization of Graphitic Carbon Nitride Sub-Microspheres Using Microwave Method under Mild Condition. *Diam. Relat. Mater.* **2013**, *38*, 109–117. https://doi.org/10.1016/J.DIAMOND.2013.06.012.

(71) Chen, L. Y.; Zhang, W. De. In2O3/g-C3N4 Composite Photocatalysts with Enhanced Visible Light Driven Activity. *Applied Surface Science.* **2014**, *301*, 428–435. https://doi.org/10.1016/J.APSUSC.2014.02.093.

(72) Wang, Z. L.; Xu, D.; Huang, Y.; Wu, Z.; Wang, L. M.; Zhang, X. B. Facile, Mild and Fast Thermal-Decomposition Reduction of Graphene Oxide in Air and Its Application in High-Performance Lithium Batteries. *Chem. Commun.* **2012**, *48* (7), 976–978. https://doi.org/10.1039/C2CC16239C.

(73) Zhang, Q.; Wang, R.; Feng, B.; Zhong, X.; Ostrikov, K. (Ken). Photoluminescence Mechanism of Carbon Dots: Triggering High-Color-Purity Red Fluorescence Emission through Edge Amino Protonation. *Nat. Commun.* **2021**, *12* (1), 1–13. https://doi.org/10.1038/s41467-021-27071-4.

(74) Dervishi, E.; Ji, Z.; Htoon, H.; Sykora, M.; Doorn, S. K. Raman Spectroscopy of Bottom-up Synthesized Graphene Quantum Dots: Size and Structure Dependence. *Nanoscale* **2019**, *11* (35), 16571–16581. https://doi.org/10.1039/c9nr05345j.

(75) Tagliaferro, A.; Rovere, M.; Padovano, E.; Bartoli, M.; Giorcelli, M. Introducing the Novel Mixed Gaussian-Lorentzian Lineshape in the Analysis of the Raman Signal of Biochar. *Nanomaterials*. **2020**; 10 (9),1748. https://doi.org/10.3390/nano10091748.

(76) Shimodaira, N.; Masui, A. Raman Spectroscopic Investigations of Activated Carbon Materials. *J. Appl. Phys.* **2002**, *92* (2), 902–909. https://doi.org/10.1063/1.1487434.

(77) Negri, F.; Di Donato, E.; Tommasini, M.; Castiglioni, C.; Zerbi, G.; Müllen, K. Resonance Raman Contribution to the D Band of Carbon Materials: Modeling Defects with Quantum Chemistry. *J. Chem. Phys.* **2004**, *120* (24), 11889–11900. https://doi.org/10.1063/1.1710853.

(78) Tuinstra F; Koenig JL. Raman Spectrum of Graphite. *J. Chem. Phys.* **1970**, *53* (3), 1126–1130. https://doi.org/10.1063/1.1674108.

(79) Petrova, E.; Tinchev, S.; Nikolova, P. Interference Effects on the ID/IG Ratio of the Raman Spectra of Diamond-like Carbon Thin Films. *Diam. Relat. Mater.* **2011**.

(80) Mewada, A.; Pandey, S.; Shinde, S.; Mishra, N.; Oza, G.; Thakur, M.; Sharon, M.; Sharon, M. Green Synthesis of Biocompatible Carbon Dots Using Aqueous Extract of Trapa Bispinosa Peel. *Mater. Sci. Eng. C* **2013**, *33* (5), 2914–2917. https://doi.org/10.1016/j.msec.2013.03.018.

(81) da Silva Souza, D. R.; Caminhas, L. D.; de Mesquita, J. P.; Pereira, F. V. Luminescent Carbon Dots Obtained from Cellulose. *Mater. Chem. Phys.* **2018**, *203*, 148–155. https://doi.org/10.1016/j.matchemphys.2017.10.001.

(82) Li, C.; Hassan, A.; Palmai, M.; Snee, P.; Baveye, P. C.; Darnault, C. J. G. Colloidal Stability and Aggregation Kinetics of Nanocrystal CdSe/ZnS Quantum Dots in Aqueous Systems: Effects of Ionic Strength, Electrolyte Type, and Natural Organic Matter. *SN Appl. Sci.* **2022**, *4* (4), 1–28. https://doi.org/10.1007/s42452-022-04948-7.

977 (83) Kamble, S.; Agrawal, S.; Cherumukkil, S.; Sharma, V.; Jasra, R. V.; Munshi, P. Revisiting
978 Zeta Potential, the Key Feature of Interfacial Phenomena, with Applications and Recent
979 Advancements. *ChemistrySelect*. **2022**, 1–40. https://doi.org/10.1002/slct.202103084.

980 (84) Glockler, G. Resonance Energies of Benzene and Butadiene. *J. Chem. Phys.* **2004**, *21* (7),
981 1249. https://doi.org/10.1063/1.1699176.

982 (85) Wang, W.; Han, J. J.; Wang, L. Q.; Li, L. S.; Shaw, W. J.; Li, A. D. Q. Dynamic π-π
983 Stacked Molecular Assemblies Emit from Green to Red Colors. *Nano Lett.* **2003**, *3* (4),
984 455–458. https://doi.org/10.1021/NL025976J.

985 (86) Liu, G.; Li, Y.; Yang, L.; Wei, Y.; Wang, X.; Wang, Z.; Tao, L. Cytotoxicity Study of
986 Polyethylene Glycol Derivatives. *RSC Adv.* **2017**, *7* (30), 18252–18259.
987 https://doi.org/10.1039/c7ra00861a.

988 (87) Zhang, M.; Li, X. H.; Gong, Y. D.; Zhao, N. M.; Zhang, X. F. Properties and
989 Biocompatibility of Chitosan Films Modified by Blending with PEG. *Biomaterials* **2002**,
990 *23* (13), 2641–2648. https://doi.org/10.1016/S0142-9612(01)00403-3.

991 (88) Meran, M.; Akkus, P. D.; Kurkcuoglu, O.; Baysak, E.; Hizal, G.; Haciosmanoglu, E.;
992 Unlu, A.; Karatepe, N.; Güner, F. S. Noncovalent Pyrene-Polyethylene Glycol Coatings of
993 Carbon Nanotubes Achieve in Vitro Biocompatibility. *Langmuir* **2018**, *34* (40), 12071–
994 12082. https://doi.org/10.1021/acs.langmuir.8b00971.

995 (89) Xu, L.; Yang, J.; Xue, B.; Zhang, C.; Shi, L.; Wu, C.; Su, Y.; Jin, X.; Liu, Y.; Zhu, X.
996 Molecular Insights for the Biological Interactions between Polyethylene Glycol and Cells.
997 *Biomaterials* **2017**, *147*, 1–13. https://doi.org/10.1016/j.biomaterials.2017.09.002.

998 (90) Priyadarshini, E.; Meena, R.; Bohidar, H. B.; Sharma, S. K.; Abdellattif, M. H.;
999 Saravanan, M.; Rajamani, P. Comparative in Vitro Cytotoxicity Study of Carbon Dot-
1000 Based Organometallic Nanoconjugates: Exploration of Their Cell Proliferation, Uptake,
1001 and Localization in Cancerous and Normal Cells. *Oxid. Med. Cell. Longev.* **2022**,
1002 https://doi.org/10.1155/2022/3483073.

1003 (91) Lewinski, N.; Colvin, V.; Drezek, R. Cytotoxicity of Nanopartides. *Small*. **2008**, 26–49.

https://doi.org/10.1002/smll.200700595.

(92) Sahu, D.; Kannan, G. M.; Tailang, M.; Vijayaraghavan, R. In Vitro Cytotoxicity of Nanoparticles: A Comparison between Particle Size and Cell Type. *J. Nanosci.* **2016**, 1–9. https://doi.org/10.1155/2016/4023852.

(93) Havrdova, M.; Hola, K.; Skopalik, J.; Tomankova, K.; Petr, M.; Cepe, K.; Polakova, K.; Tucek, J.; Bourlinos, A. B.; Zboril, R. Toxicity of Carbon Dots-Effect of Surface Functionalization on the Cell Viability, Reactive Oxygen Species Generation and Cell Cycle. *Carbon N. Y.* **2016**, *99*, 238–248. https://doi.org/10.1016/j.carbon.2015.12.027.

(94) Werle, M. Natural and Synthetic Polymers as Inhibitors of Drug Efflux Pumps. *Pharm. Res.* **2008**, *25* (3), 500. https://doi.org/10.1007/S11095-007-9347-8.

(95) Johnson, B. M.; Charman, W. N.; Porter, C. J. H. An in Vitro Examination of the Impact of Polyethylene Glycol 400, Pluronic P85, and Vitamin E d-Alpha-Tocopheryl Polyethylene Glycol 1000 Succinate on P-Glycoprotein Efflux and Enterocyte-Based Metabolism in Excised Rat Intestine. *AAPS PharmSci* **2002**, *4* (4). https://doi.org/10.1208/PS040440.

(96) Fogal, V.; Zhang, L.; Krajewski, S.; Ruoslahti, E. Mitochondrial/Cell-Surface Protein P32/GC1qR as a Molecular Target in Tumor Cells and Tumor Stroma. *Cancer Res.* **2008**, *68* (17), 7210–7218. https://doi.org/10.1158/0008-5472.CAN-07-6752.

(97) Simón-Gracia, L.; Sidorenko, V.; Uustare, A.; Ogibalov, I.; Tasa, A.; Tshubrik, O.; Teesalu, T. Novel Anthracycline Utorubicin for Cancer Therapy. *Angew. Chemie - Int. Ed.* **2021**, *60* (31), 17018–17027. https://doi.org/10.1002/anie.202016421.

(98) d'Avanzo, N.; Torrieri, G.; Figueiredo, P.; Celia, C.; Paolino, D.; Correia, A.; Moslova, K.; Teesalu, T.; Fresta, M.; Santos, H. A. LinTT1 Peptide-Functionalized Liposomes for Targeted Breast Cancer Therapy. *Int. J. Pharm.* **2021**, *597*. https://doi.org/10.1016/j.ijpharm.2021.120346.

(99) Ferreira, B. C. L. B.; Liyanage, P. Y.; Leblanc, R. M. Drug Loading of Anthracycline Antibiotics on Carbon Dots Using Circular Dichroism Spectrometry. *Anal. Chem.* **2021**,

93 (44), 14773–14777. https://doi.org/10.1021/acs.analchem.1c03385.

(100) Woody, R. W. Circular Dichroism. *Methods Enzymol.* **1995**, *246* (C), 34–71. https://doi.org/10.1016/0076-6879(95)46006-3.

(101) Strub, C.; Alies, C.; Lougarre, A.; Ladurantie, C.; Czaplicki, J.; Fournier, D. Mutation of Exposed Hydrophobic Amino Acids to Arginine to Increase Protein Stability. *BMC Biochem.* **2004**, *5* (1), 1–6. https://doi.org/10.1186/1471-2091-5-9.

(102) Das, S.; Lin, Y. H.; Vernon, R. M.; Forman-Kay, J. D.; Chan, H. S. Comparative Roles of Charge, π, and Hydrophobic Interactions in Sequence-Dependent Phase Separation of Intrinsically Disordered Proteins. *Proc. Natl. Acad. Sci. U. S. A.* **2020**, *117* (46), 28795–28805. https://doi.org/10.1073/pnas.2008122117.

(103) Timasheff, S. N. Solvent Stabilization of Protein Structure. *Methods in molecular biology* **1995**, 253–269. https://doi.org/10.1385/0-89603-301-5:253.

(104) Paudyal, S.; Sharma, S. K.; da Silva, R. L. C. G.; Mintz, K. J.; Liyanage, P. Y.; Al-Youbi, A. O.; Bashammakh, A. S.; El-Shahawi, M. S.; Leblanc, R. M. Tyrosinase Enzyme Langmuir Monolayer: Surface Chemistry and Spectroscopic Study. *J. Colloid Interface Sci.* **2020**, *564*, 254–263. https://doi.org/10.1016/j.jcis.2019.12.118.

(105) da Silva, R. L. C. G.; Sharma, S. K.; Paudyal, S.; Mintz, K. J.; Caseli, L.; Leblanc, R. M. Surface Chemistry and Spectroscopic Studies of the Native Phenylalanine Dehydrogenase Langmuir Monolayer at the Air/Aqueous NaCl Interface. *J. Colloid Interface Sci.* **2020**, *560*, 458–466. https://doi.org/10.1016/j.jcis.2019.10.086.

(106) Micsonai, A.; Wien, F.; Kernya, L.; Lee, Y. H.; Goto, Y.; Réfrégiers, M.; Kardos, J. Accurate Secondary Structure Prediction and Fold Recognition for Circular Dichroism Spectroscopy. *Proc. Natl. Acad. Sci. U. S. A.* **2015**, *112* (24), E3095–E3103. https://doi.org/10.1073/pnas.1500851112.

(107) Micsonai, A.; Bulyáki, É.; Kardos, J. BeStSel: From Secondary Structure Analysis to Protein Fold Prediction by Circular Dichroism Spectroscopy. In *Methods in Molecular Biology*. **2021**, 2199, 175–189. https://doi.org/10.1007/978-1-0716-0892-0_11.

(108) Micsonai, A.; Wien, F.; Bulyáki, É.; Kun, J.; Moussong, É.; Lee, Y. H.; Goto, Y.; Réfrégiers, M.; Kardos, J. BeStSel: A Web Server for Accurate Protein Secondary Structure Prediction and Fold Recognition from the Circular Dichroism Spectra. *Nucleic Acids Res.* **2018**, *46* (W1), W315–W322. https://doi.org/10.1093/nar/gky497.

(109) Brightman, M. W.; Reese, T. S. Junctions between Intimately Apposed Cell Membranes in the Vertebrate Brain. *J. Cell Biol.* **1969**, *40* (3), 648–677. https://doi.org/10.1083/jcb.40.3.648.

(110) Huang, H. Y.; Liu, H. L.; Hsu, P. H.; Chiang, C. S.; Tsai, C. H.; Chi, H. S.; Chen, S. Y.; Chen, Y. Y. A Multitheragnostic Nanobubble System to Induce Blood-Brain Barrier Disruption with Magnetically Guided Focused Ultrasound. *Adv. Mater.* **2015**, *27* (4), 655–661. https://doi.org/10.1002/adma.201403889.

(111) Li, S.; Peng, Z.; Dallman, J.; Baker, J.; Othman, A. M.; Blackwelder, P. L.; Leblanc, R. M. Crossing the Blood-Brain-Barrier with Transferrin Conjugated Carbon Dots: A Zebrafish Model Study. *Colloids Surfaces B Biointerfaces* **2016**, *145*, 251–256. https://doi.org/10.1016/j.colsurfb.2016.05.007.

(112) Panula, P.; Sallinen, V.; Sundvik, M.; Kolehmainen, J.; Torkko, V.; Tiittula, A.; Moshnyakov, M.; Podlasz, P. Modulatory Neurotransmitter Systems and Behavior: Towards Zebrafish Models of Neurodegenerative Diseases. *Zebrafish*. **2006**, 235–247. https://doi.org/10.1089/zeb.2006.3.235.

(113) Aceto, J.; Nourizadeh-Lillabadi, R.; Marée, R.; Dardenne, N.; Jeanray, N.; Wehenkel, L.; Aleström, P.; Van Loon, J. J. W. A.; Muller, M. Zebrafish Bone and General Physiology Are Differently Affected by Hormones or Changes in Gravity. *PLoS One* **2015**, *10* (6), e0126928. https://doi.org/10.1371/journal.pone.0126928.

(114) Jeong, J. Y.; Kwon, H. B.; Ahn, J. C.; Kang, D.; Kwon, S. H.; Park, J. A.; Kim, K. W. Functional and Developmental Analysis of the Blood–Brain Barrier in Zebrafish. *Brain Res. Bull.* **2008**, *75* (5), 619–628. https://doi.org/10.1016/J.BRAINRESBULL.2007.10.043.

(115) Xu, K. F.; Jia, H. R.; Wang, Z.; Feng, H. H.; Li, L. Y.; Zhang, R.; Durrani, S.; Lin, F.; Wu, F. G. See the Unseen: Red-Emissive Carbon Dots for Visualizing the Nucleolar Structures in Two Model Animals and In Vivo Drug Toxicity. *Small* **2023**, 2205890. https://doi.org/10.1002/smll.202205890.

(116) Xu, Y.; Wang, C.; Sui, L.; Ran, G.; Song, Q. Phosphoric Acid Densified Red Emissive Carbon Dots with a Well-Defined Structure and Narrow Band Fluorescence for Intracellular Reactive Oxygen Species Detection and Scavenging. *J. Mater. Chem. C* **2023**, *11* (8), 2984–2994. https://doi.org/10.1039/d2tc04897c.

(117) Zhu, Z.; Zhai, Y.; Li, Z.; Zhu, P.; Mao, S.; Zhu, C.; Du, D.; Belfiore, L. A.; Tang, J.; Lin, Y. Red Carbon Dots: Optical Property Regulations and Applications. *Materials Today*. **2019**,52–79. https://doi.org/10.1016/j.mattod.2019.05.003.

(118) Hussain, M. M.; Khan, W. U.; Ahmed, F.; Wei, Y.; Xiong, H. Recent Developments of Red/NIR Carbon Dots in Biosensing, Bioimaging, and Tumor Theranostics. *Chemical Engineering Journal*. **2023**, 143010. https://doi.org/10.1016/j.cej.2023.143010.

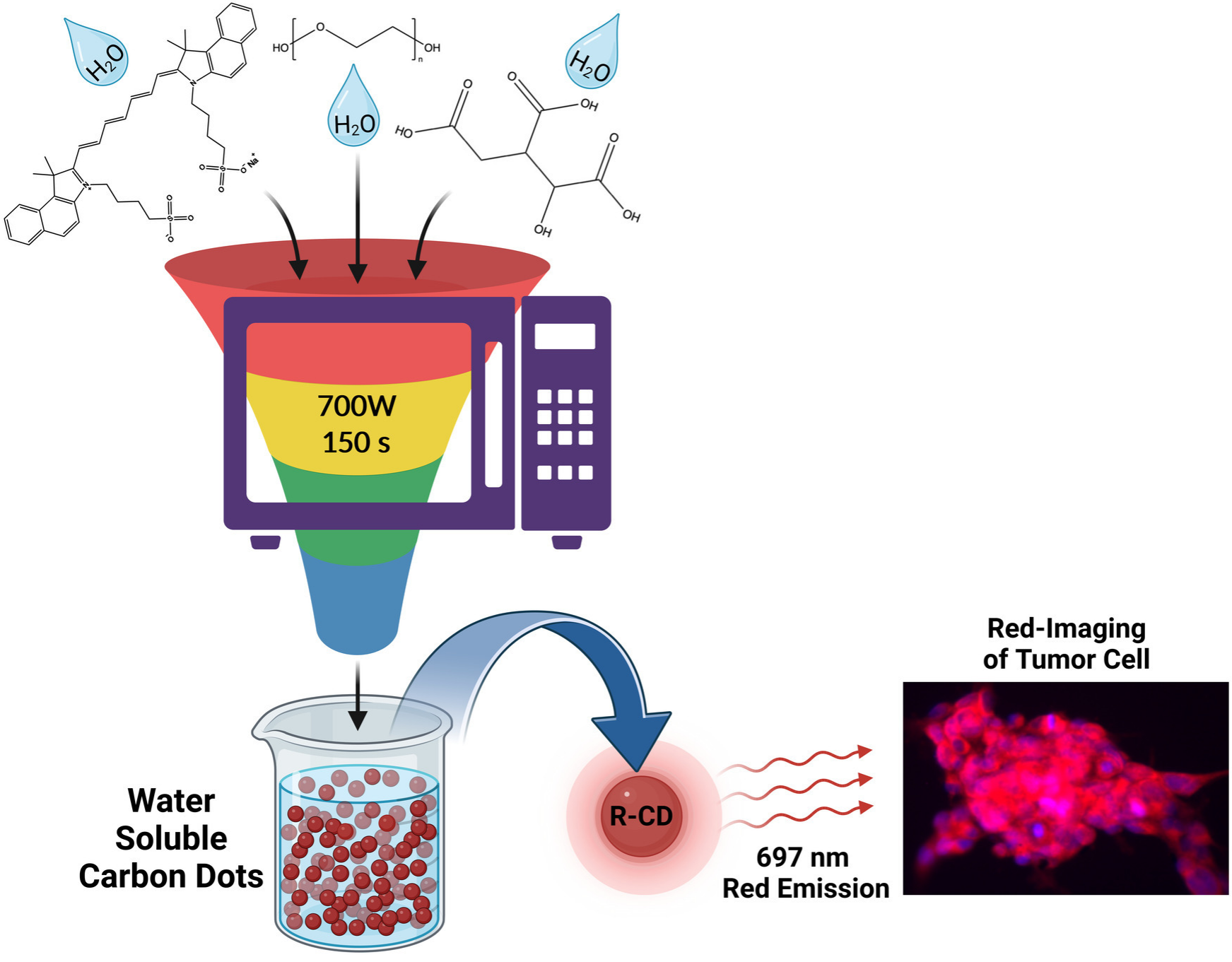
H2O
H2O
H2O
700W
150 s
Water
Soluble
Carbon Dots
R-CD
697 nm
Red Emission
Red-Imaging
of Tumor Cell